Chapter 3

Historical

This chapter examines the history and evolution of modern seismic migration methods. Modern migration methods evolved from simple geometric concepts to complex wave-equation techniques. The major driving force for such dynamic changes is the overwhelming need to transition from doing calculations using pencils and paper to analog calculators and finally to modern digital computers. This section reviews that process and provides a firm foundation for the geometric concepts that led to the modern era.

It should be noted that modern geophysical mathematical concepts governing wave propagation in complex geologic media have been studied and developed before the current epoch. Many of these theories date back to the early 20th, the 19th, and even, in some cases, the late 18th centuries. While the scientific foundations were definitely available, many early geophysical explorationists tended to ignore them and rely instead on what might be called more *ad hoc* methodologies. What we use today is the result of a lengthy trial and error stumble urged on by the need to find hydrocarbons hidden in more and more difficult to find traps.

Data Acquisition

During World War I (1914-1918), sound waves from exploding bombs and other ordinance were detected many miles from the explosion point. Noise from the operation of submarines was detected over even greater distances. These two observable events are thought to have lead to the speculation that one could detect geologic bedding planes by recording the sound energy from a surface explosion. Oil companies around the world began to research whether or not such an idea might be possible. One of the early investigators into this idea was a physicist named Reginald Fessenden. Figure 3-1 describes Fessenden’s scheme for locating geological formations using a sound source. The source in this case was essentially a vibrator not unlike what we call a vibroseis today. The technique is also virtually identical to what would ultimately became sonar for locating submerged submarines.

Figure 3-1. A graphic describing the essence of R. Fessenden’s 1917 patent for devices to generate and record seismic energy.

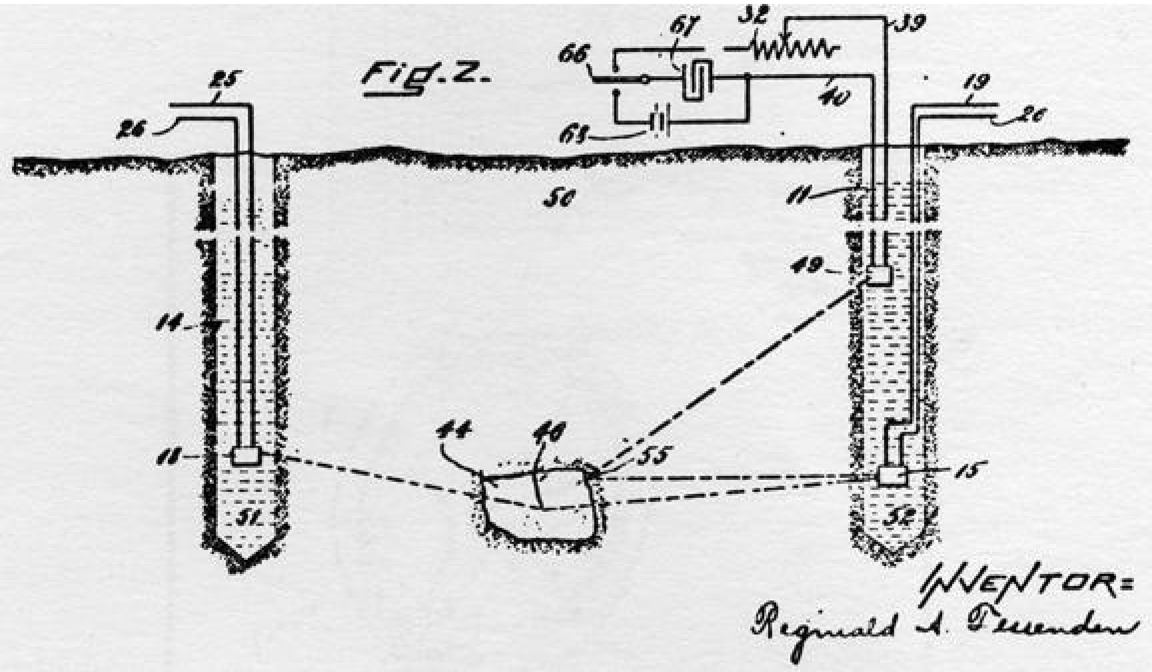

While I am quite sure that Fessenden was completely convinced that his device would work, his belief was not shared by all. Thus, it was necessary to prove empirically that a surface sound source would generate reflections from geologic formations, and that such reflections could be recorded at the surface and mapped or interpreted to find hydrocarbon bearing traps.

At this point in time, making a microphone, or what we now call a geophone, was very expensive and each such device was very heavy. Thus, in the very early days, very few receivers were used to record the response of each shot. Figure 3-2 shows a typical four microphone recording from 1928. It is believed to be one of the first seismic recordings to empirically verify that reflections from subsurface formations occurred and could be detected. The large oscillations at the beginning of this shot profile indicate the first arrival of energy from the source. The arrival indicated by the arrow as well as those above it are all reflections from the Cimarron anhydrite in central Kansas on the Seminole Plateau. The fact that these amplitudes were actually reflections was verified by drilling a well at the end of a line of four receiver shots.

Figure 3-2. A single trace recording

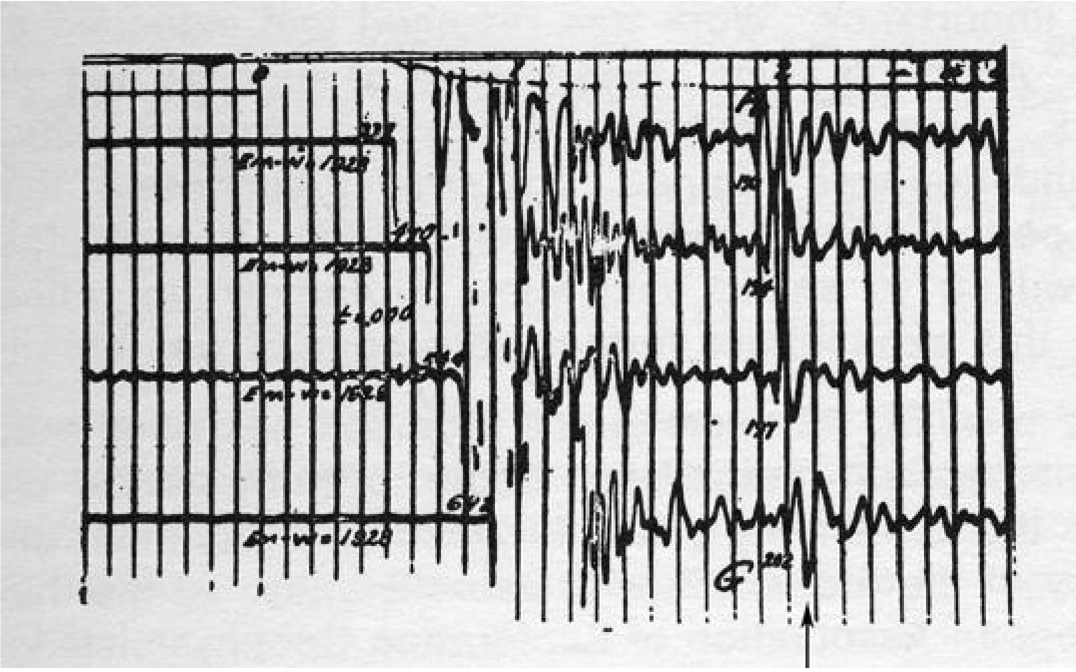

Zero Offset Hand Migration

Given records like that in Figure 3-2, early explorers made a *stickmap* that might have looked something like the one displayed in Figure 3-3. The times defining the event in this figure would most likely have been based on the identified arrival from the closest trace to the shot point. They would have liked to have a trace in which the shot and receiver were coincident. But, because they were using dynamite, this would have resulted in the destruction of the receiver, and so they settled for receivers that were close to the shot. In Figure 3-2, the closest trace would have been the time pointed to by the arrow with a shot-receiver separation (offset) of about 100 meters. This separation would have to suffice as an approximation to a trace with coincident source and receiver. Such traces were called zero-offset traces.

Figure 3-3. A simple non-flat horizon

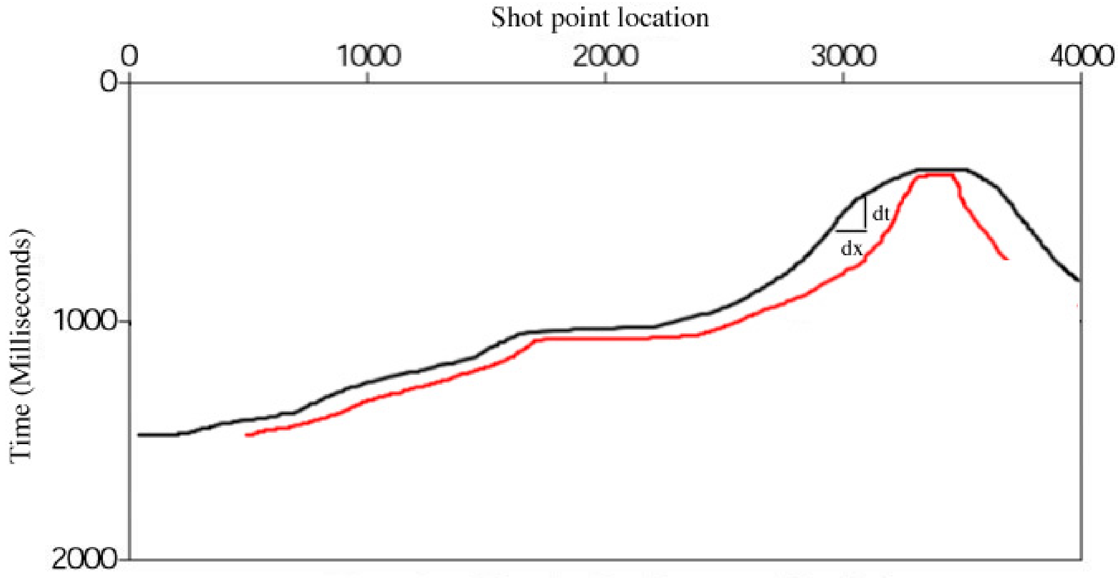

The black line graph in Figure 3-3 represents what is called a zero-offset or unmigrated time *section*. What is necessary for exploration and drilling is a depth map, or, when the velocity is constant, a migrated time map as conceptualized by the red line graph. In this case, the red line was simply drawn in free-hand, but represents the major features of what might be the true migration position of a reflected horizon. Note in particular that after migration, the peak of the anticline has not changed position, but its width has shrunk. It is also true that the positions of dipping events have moved up-dip in every case.

To produce the red-line section in Figure 3-3, we need to know how to convert unmigrated arrivals into migrated arrivals. Figure 3-4 shows the relationship between zero-offset reflections and their correct migrated position. The true reflector has a true dip angle of α, while the apparent or recorded event is at dip angle β. In this figure, the data is assumed to have been recorded over a constant velocity medium. Note that the location of the migrated event is placed relative to vertical time or depth, but remember that this vertical positioning is only valid for constant velocity media. Since the velocity is constant, vertical depth is given formally by the traditional relationship, where depth is equal to velocity times one-way time, that is, $d = vt/2$ or $t = 2d/v$.

Figure 3-4. Fundamental migration geometry between the apparent location and dip β versus the migrated location and dip α.

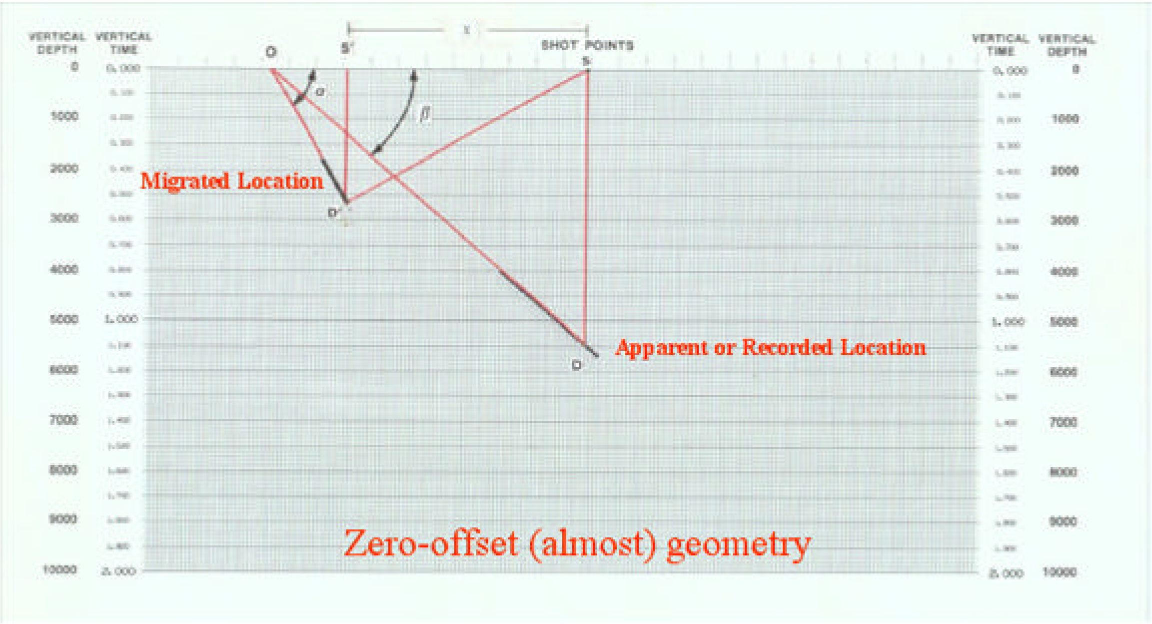

Migration in a two-dimensional, constant velocity medium requires only that we know the sound speed in the medium, and can measure the ratio of the change in arrival time to the corresponding horizontal change. As indicated in Figure 3-5, this is usually specified in seconds per trace divided by the trace spacing, but any time interval and corresponding spatial interval will do. The formulas listed in the figure provide all necessary calculations to determine the migrated position of any given event. Note again that in this simple medium, vertical depth is easily obtained by multiplying the vertical time, t, by the medium sound speed, v. Note also that events with any given apparent dip migrate up-dip. Consequently, we can ignore the sign of any given value and simply place the migrated dip element at its appropriate up-dip position. As we will see, extension of this formula to a vertically varying medium is quite easy.

Figure 3-5. Fundamental migration trigonometry relating the apparent location and dip specified by S and β versus the migrated location and dip specified by S' and α.

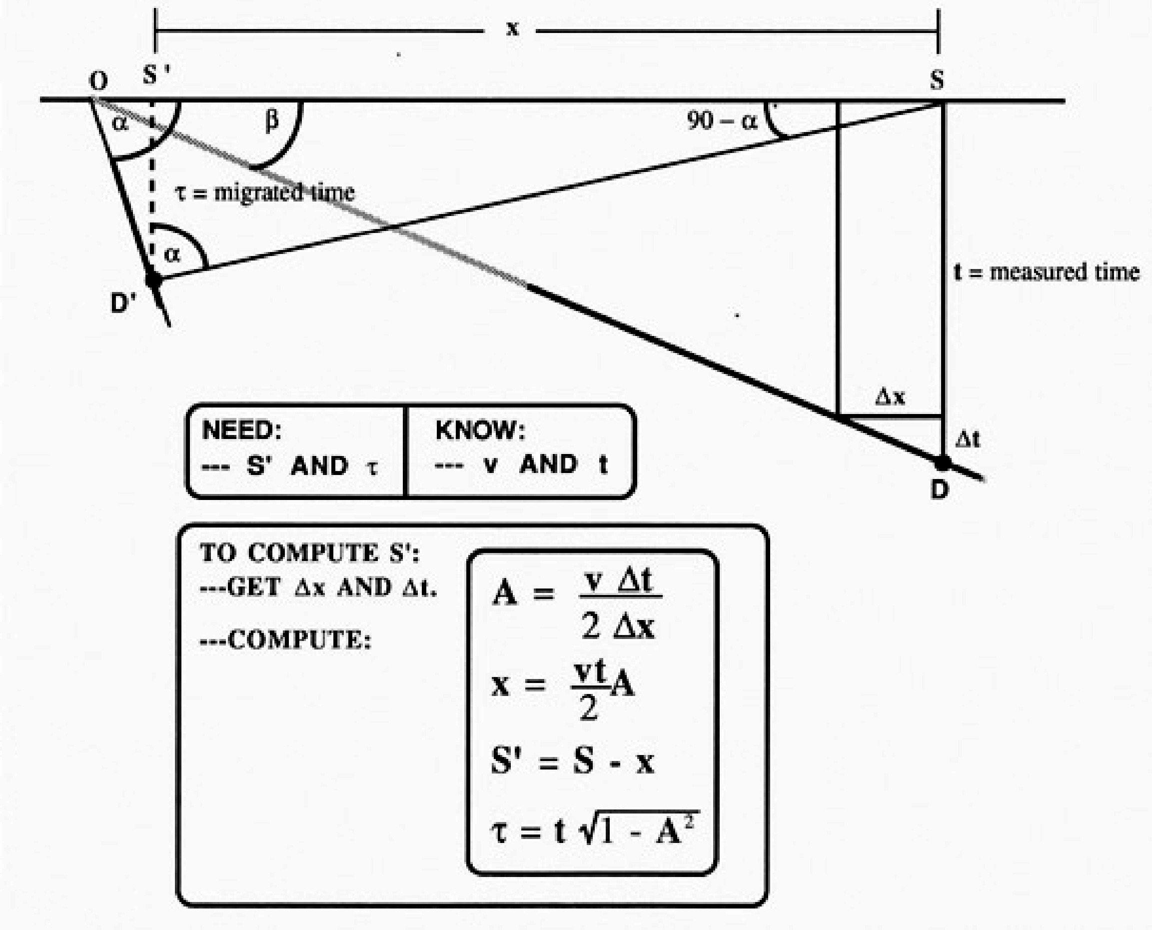

Figure 3-6 extends the migration formulas in Figure 3-5 to a three-dimensional constant-velocity medium. These equations provide the necessary computational formulas to complete the migration process. Here, however, it is a bit more difficult to actually do the migration by hand. At this point, the migrated position must be contoured to produce a migrated map of the recorded event.

Figure 3-6. Fundamental migration trigonometry relating the apparent location and dip specified by the S and β versus the migrated location and dip specified by S' and α.

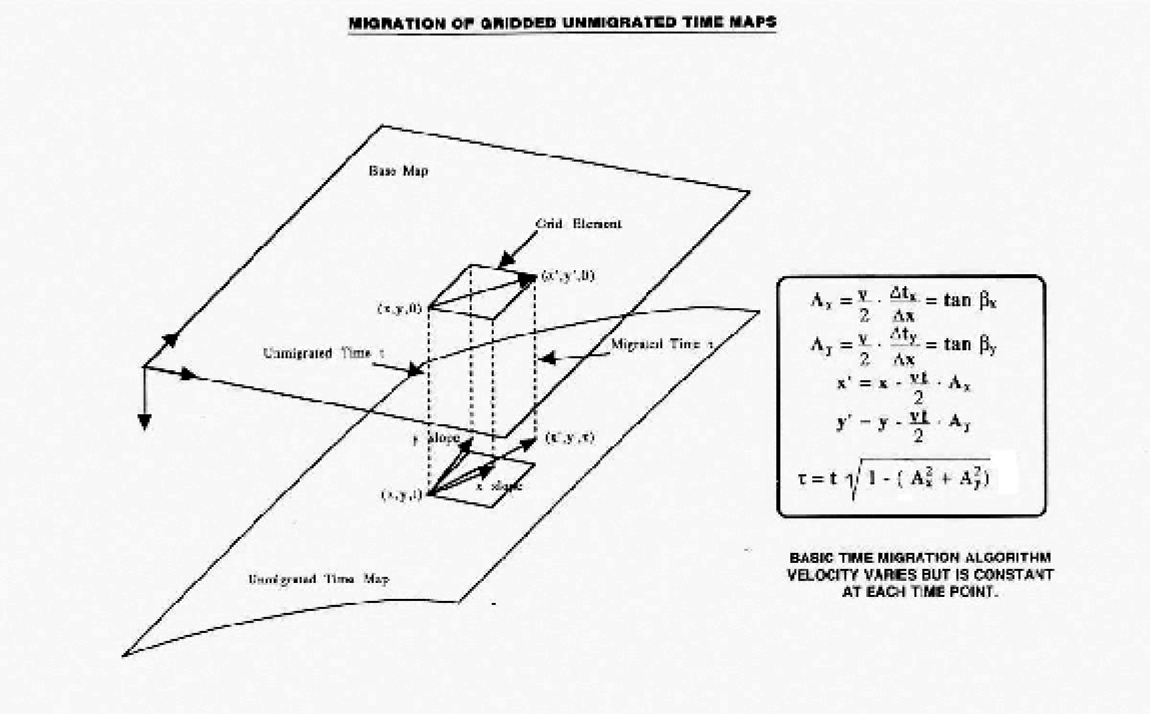

Beginning in the late 1940's and continuing until the early 1960's, all interpreters used this approach to produce migrated prospect maps. The equations were employed in a two-step manner, where calculations proceeded in the line direction, and were then followed by similar calculations in the cross-line direction.

Figure 3-7 shows an example of an unmigrated or zero-offset map. This map is from an early interpretation done over a salt dome in the Gulf of Mexico at South Pass Block 89. Faults and the large truncation surrounding the large salt dome are clearly evident.

Figure 3-7. An unmigrated (zero-offset) time map of a salt structure in the Gulf of Mexico. This particular map was contoured in 1972 or 1973 from a two-dimensional grid.

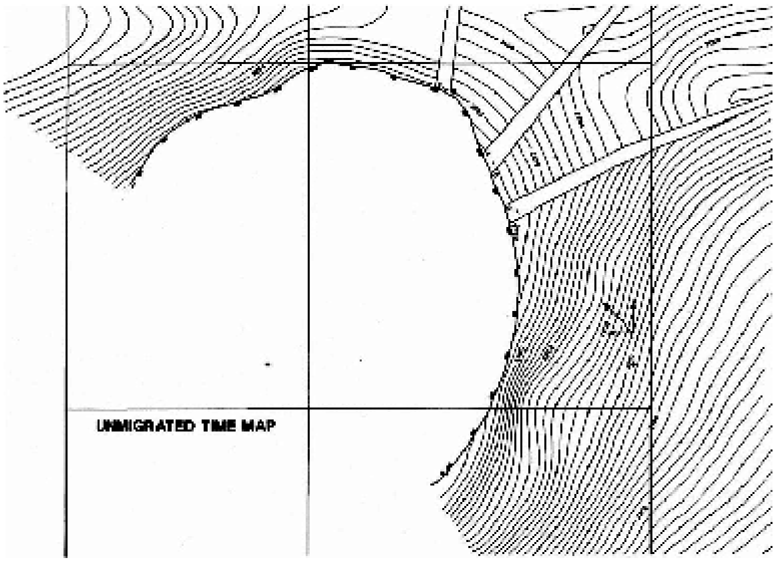

The vectors graphed in Figure 3-8 are the result of using the equations in Figure 3-6. A computer was used to generate and plot the vectors. Note the significant change in the shape of the salt structure and note also that some of these vectors are over two miles in length. It is important to observe that any 2D migration of the red line will be inaccurate. Not only does its subsurface position migrate up-dip, but its shape can change quite dramatically. This is a basic reason why 3D imaging is so superior to 2D.

Figure 3-8. Migrated vectors from the map in Figure 3-7 computed using the formulas in Figure 3-6.

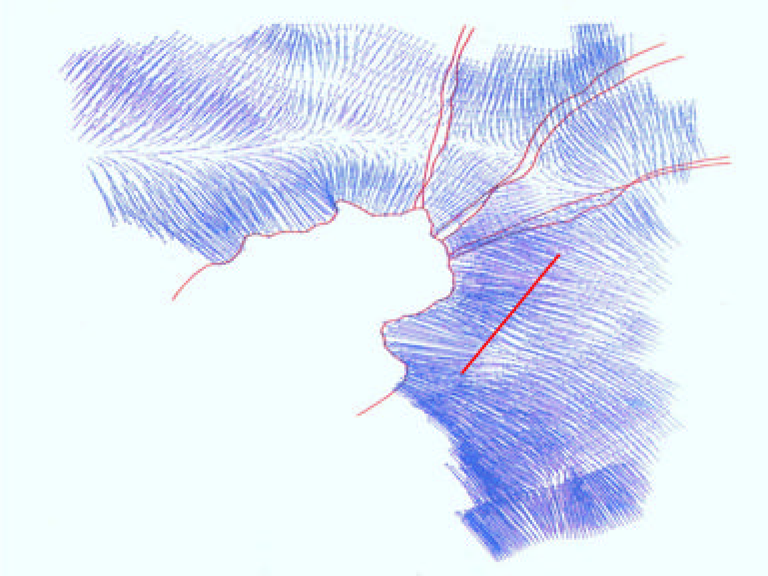

Shot Profile Hand Migration in Two Dimensions

Picking traveltimes from a short-offset trace to approximate zero-offset arrivals and thereby produce a zero-offset section works well when neither the velocity nor the geometry of the local formations vary dramatically. It breaks down when velocity variation is strong, when the structure of the subsurface horizons is complex and when assuring that the current pick is on the same formation as the last pick is difficult.

The first approach to alleviating at least some of these problems was to increase the number of geophones in each shot profile. Instead of using a handful of receivers on one side of a shot, “split-spread” shooting, as shown in Figure 3-9, became prominent. After each shot was recorded into multiple receivers, one half of the receivers were picked up and moved to produce a new split-spread array for the next shot. For example, in the diagram in this figure, the receivers on the left would be moved so that the left-most receiver is just to the right of the right-most receiver. A new source would be discharged and recorded into the newly positioned array. As this process continued, complete coverage of the subsurface reflector is accomplished. As shown in the left hand trace graphic in Figure 3-10, trace-to-trace correlation is now much easier, and subsurface mapping is supposedly simplified.

Figure 3-9. A typical 2D shot diagram from the mid 1960's to around 1975. These were used in split-spread shooting arrangements.

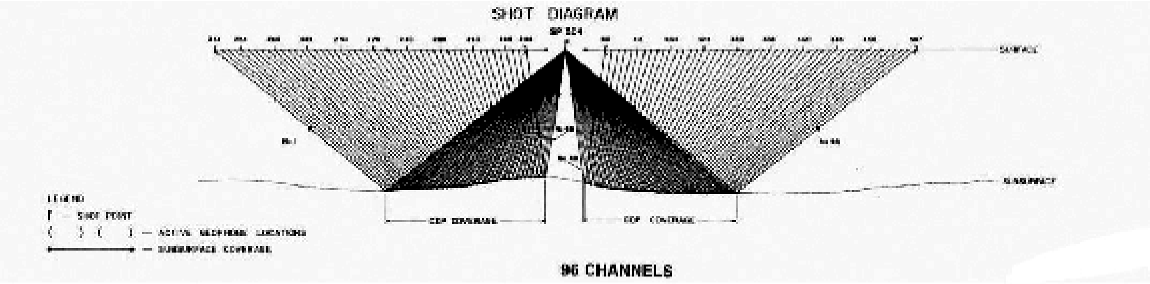

Figure 3-10. Detecting dip. The amplitude and direction were defined by a slant stack.

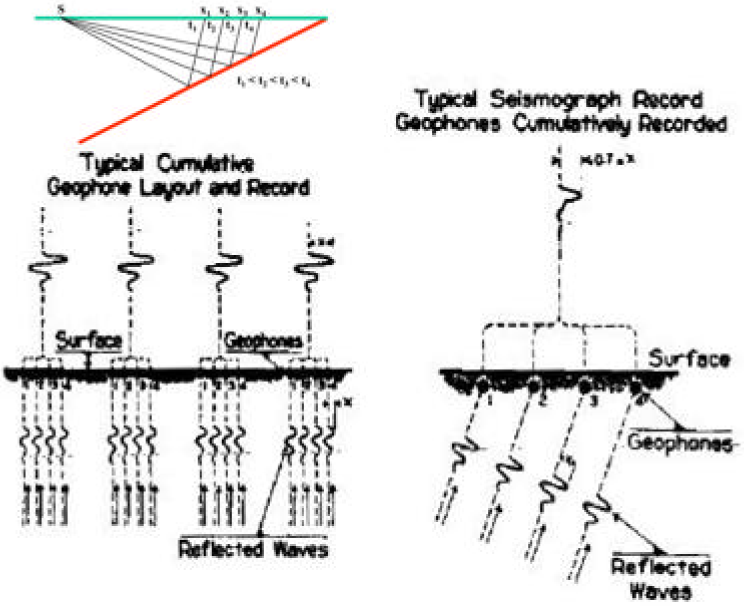

A key question that needed an answer was what does dip really look like on a shot record with a large number of receivers. Could shot-record dip be used to estimate the location of the reflecting horizon?

These questions were not focused so much on dip, but on whether or not you could estimate the dip from the shot profile and then figure out where the reflection came from. Figure 3-10 shows Rieber's 1936 solution to the question of estimating dip. He delayed each shot linearly (right hand side of the figure) and summed up the amplitudes. When a large amplitude was found, the delay required to find it defined the emergence angle, and so gave insight into both the arrival direction and the amount of subsurface dip that produced it. He was probably the first to recognize the importance of summing over lines (slant stacks) to reduce the problem to one of simply detecting an amplitude.

Unfortunately, I am not aware of anyone who took advantage of Rieber's methods in any detail during his day. It was not until the advent of modern computers that his method came to the forefront in the form of plane-wave or beam stack approaches to imaging. However, using information from a shot profile still became a viable approach to more accurate subsurface mapping.

Figure 3-11 shows what an aspiring geophysicist named Klaus Helbig was given as a test in 1952. It was his introduction to geophysics. He is a well known German geophysicist who is still alive at this writing and is a wonderful source of historical information about how geophysics was done prior to the advent of powerful computers. I am indebted to him for many of the figures and exercises in this section. Figure 3-11 shows a synthetic shot profile on the right. The problem, given an assumed velocity of 3000 meters per second, is to find the reflection point that generated the shot record on the right. As described in Figure 3-12, the problem is easily solved by applying Pythagorus' theorem, and Figure 3-13 provides the numerical answer to the problem. This calculation requires close attention to the different signs, but essentially everything still moves up dip. Even at the modest production rates of the fifties, it was unavoidable that errors crept into the several hundred calculations that had to be performed by hand. As Helbig says:

> Other companies must have had their way of dealing with this problem. In our company, a two-dimensional slide rule was used. While it was not absolutely fool proof, it simplified the calculations drastically and forced the operator to be consistent. Consistent sign errors are more easily detected than random errors.

Figure 3-11. A test for an aspiring geophysicist.

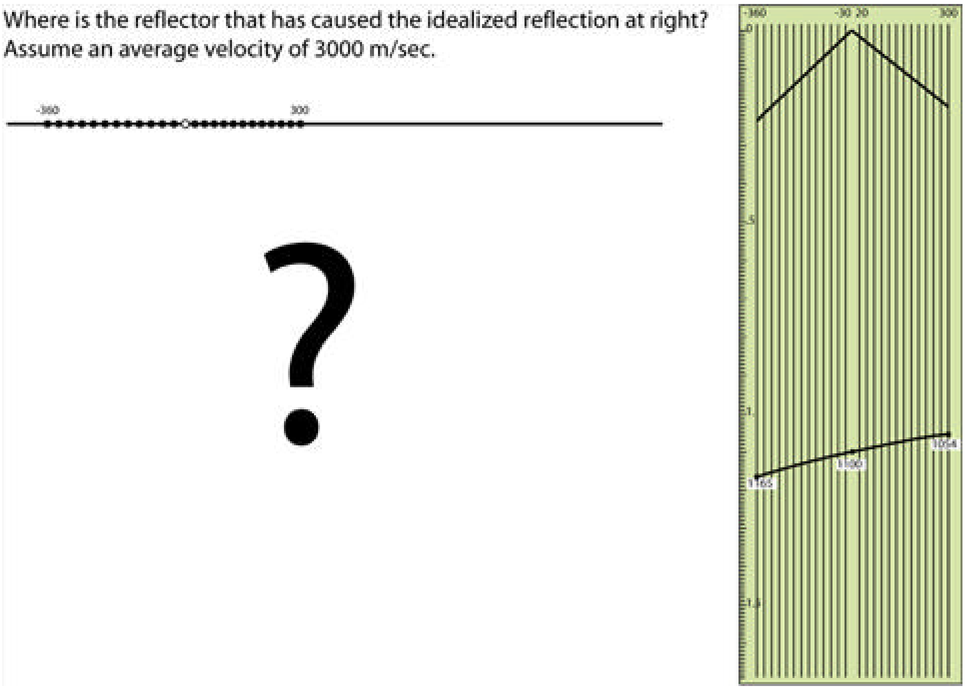

Where is the reflector that has caused the idealized reflection at right?
Assume an average velocity of 3000 m/sec.

Figure 3-12. Klaus Helbig's solution to the problem of Figure 3-11.

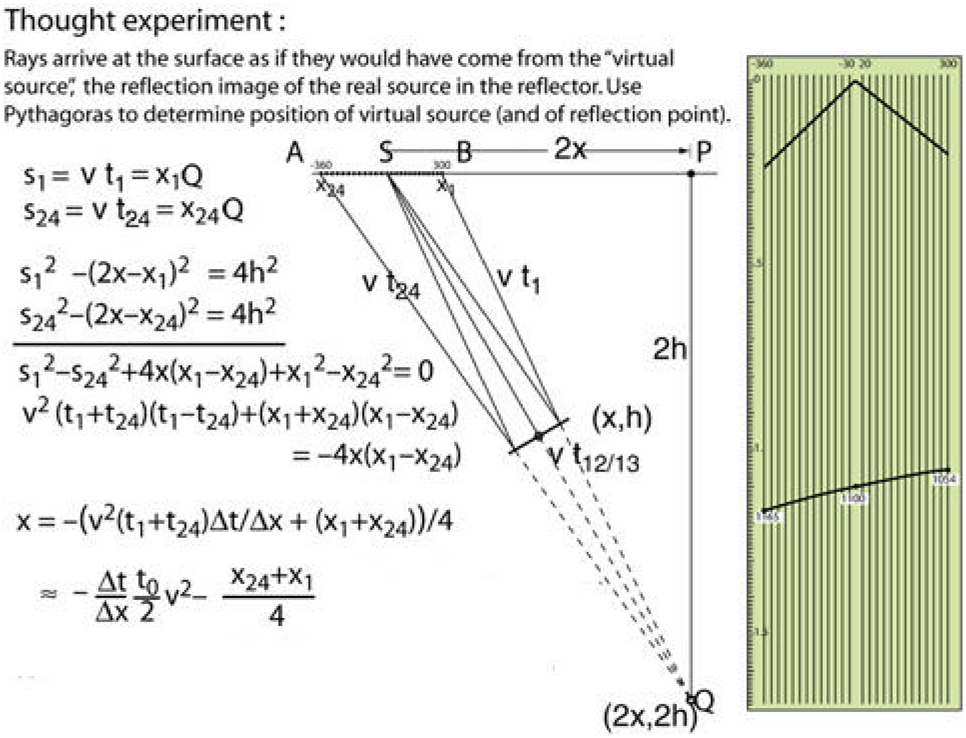

Thought experiment :

Rays arrive at the surface as if they would have come from the "virtual source", the reflection image of the real source in the reflector. Use Pythagoras to determine position of virtual source (and of reflection point).

$$s_1 = v\,t_1 = x_1Q$$
$$s_{24} = v\,t_{24} = x_{24}Q$$
$$s_1^2 - (2x-x_1)^2 = 4h^2$$
$$s_{24}^2 - (2x-x_{24})^2 = 4h^2$$
$$s_1^2 - s_{24}^2 + 4x(x_1-x_{24}) + x_1^2 - x_{24}^2 = 0$$
$$v^2(t_1+t_{24})(t_1-t_{24}) + (x_1+x_{24})(x_1-x_{24}) = -4x(x_1-x_{24})$$
$$x = -(v^2(t_1+t_{24})\Delta t/\Delta x + (x_1+x_{24}))/4$$
$$\approx -\frac{\Delta t}{\Delta x}\frac{t_0}{2}v^2 - \frac{x_{24}+x_1}{4}$$

Figure 3-13. The numerical solution to the problem in Figure 3-11.

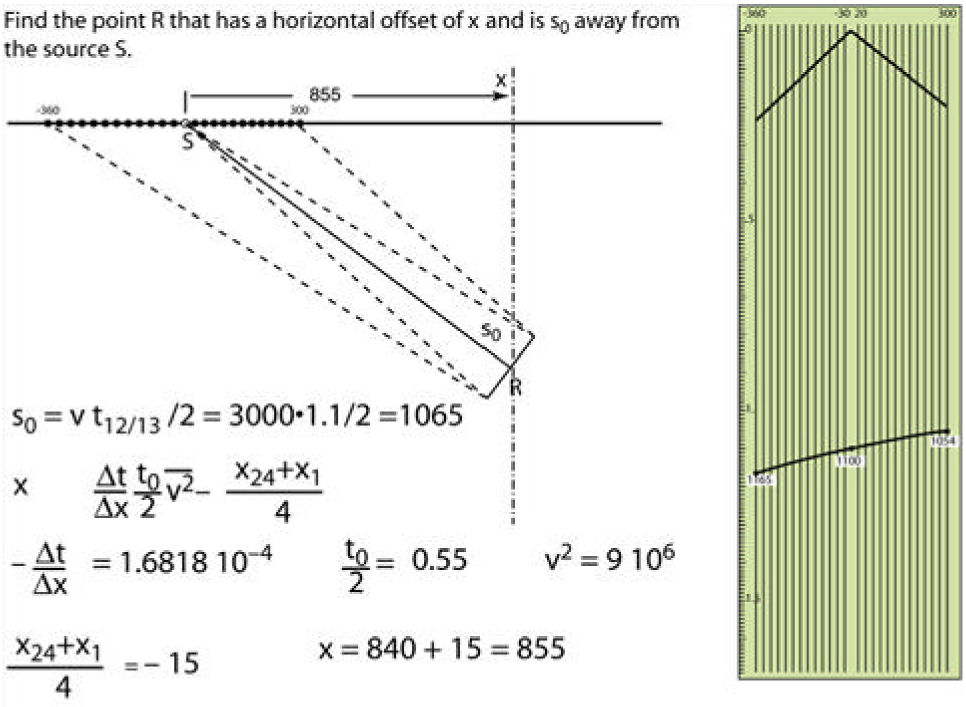

Find the point R that has a horizontal offset of x and is s_0 away from the source S.

$$s_0 = v\,t_{12/13}/2 = 3000\cdot1.1/2 = 1065$$
$$x \quad \frac{\Delta t}{\Delta x}\frac{t_0}{2}v^2 - \frac{x_{24}+x_1}{4}$$
$$-\frac{\Delta t}{\Delta x} = 1.6818\;10^{-4} \qquad \frac{t_0}{2} = 0.55 \qquad v^2 = 9\;10^6$$
$$\frac{x_{24}+x_1}{4} = -15 \qquad x = 840 + 15 = 855$$

It is worth noting that we can use virtually any two picks from the shot record displayed in Figures 3-11, 3-12, and 3-13 to perform a migration. Such picks can be from any pair of traces within the shot profile, so, technically speaking, we can migrate the shot record in a very detailed manner. It is also worth mentioning that what is happening is shot-by-shot migration. It was done by humans as opposed to a digital computer, but it is still a shot-by-shot or shot profile migration.

Performing the computations involved in migration by hand is clearly difficult. Even in two-dimensions, this process was fraught with error. As a result, there was a strong push to automate the process to be able to choose well locations quickly and more accurately. One of the first such devices, as shown schematically in Figure 3-14, might best be described as a plotting device.

Figure 3-14. A simple machine for drawing reflectors at positions determined by the solution to Klaus Helbig's "thought problem."

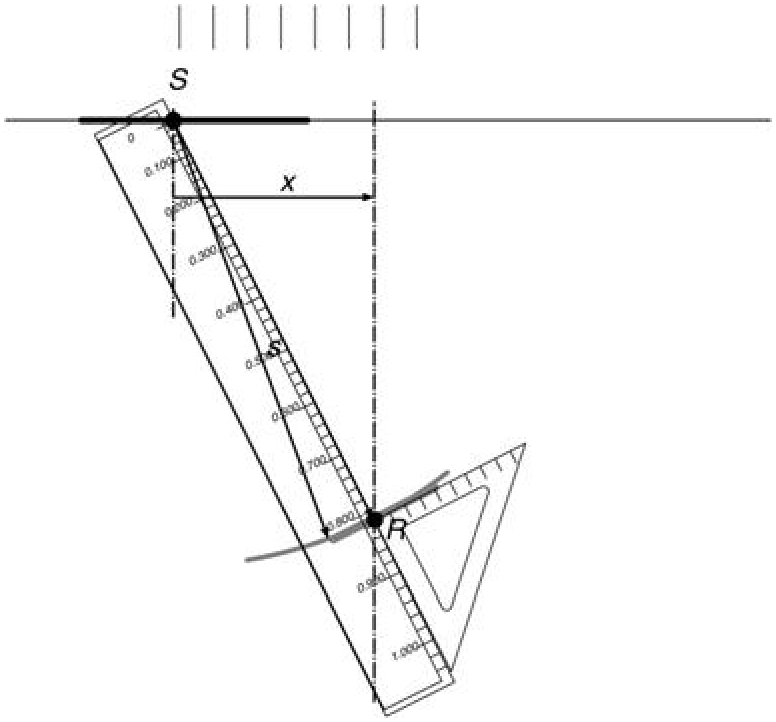

As drawn, it cannot directly calculate the value of x (Equation 3-1) in Figure 3-12, but given a bit of experience by the interpreter, it can produce very accurate *stickmap* interpretations of true subsurface horizon locations.

(3-1)

$$x = \frac{\Delta t}{\Delta x}\frac{t_0}{2}v^2 - \frac{x_{24} + x_1}{4}$$

Again, according to Klaus:

> A temporary vertical line is drawn at horizontal distance x down to the (expected) position of the reflector element. A ruler graduated in distance traveled for given times (times are displayed on the scale) is placed so that the zero-mark is at the source S and the actual traveltime at the intersection with the temporary vertical line. With the ruler firmly held in place, a small set square is placed against the ruler to draw the forward part of the reflector elements. The set square is graduated at half the scale of the rest of the drawing. This simplifies the drawing of the lengths of the parts of the reflector elements (about half as long as the corresponding surface spreads).

While it is not really a migration machine, it does foretell the kind of device that would follow to reduce the computational complexities associated with the constant velocity and straight ray formula of Figure 3-12.

Curved Rays

Until this point in time, rays underlying seismic imaging were implicitly assumed to be straight. Allowing the velocities in our Earth model to vary requires that we allow rays to refract or bend. The concept is illustrated in the cartoon of Figure 3-15. Because light travels at different speeds in air and water, it refracts. Thus, the bowman must shoot below the image of the fish he sees in the water to hit it. When velocities vary significantly, failure to accurately account for reflections along bent rays can cause significant misplacement of subsurface events. This is particularly true in subsalt plays, but is generally true for almost all prospective areas. When this was recognized, migrations began to enter what might be called the depth era. Doing this properly increased the need for a more automated method for producing the stick map images.

Figure 3-15. Fishing with a bow and arrow

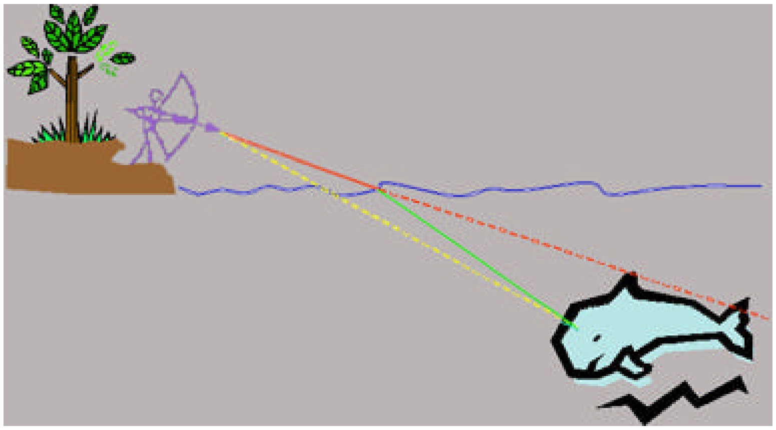

If the bowman is to hit the fish, he must properly account for the way in which light refracts as it passes from the water into the air. Similarly, the seismic program must account for the way sound is refracted when it passes from one layer to another. Both processes, in fact, obey Snell's law, which states that the ratio of the sines of the angles of incidence and refraction is equivalent to the ratio of velocities in the two media, and is also equivalent to the inverse of the ratio of the indices of refraction. For example, when a sound wave is reflected from *R* in Figure 3-16 and travels toward the surface, it is transmitted through each layer according to Snell's law. This relationship is stated mathematically in Equation 3-2.

Figure 3-16. Illustration of Snell's Law

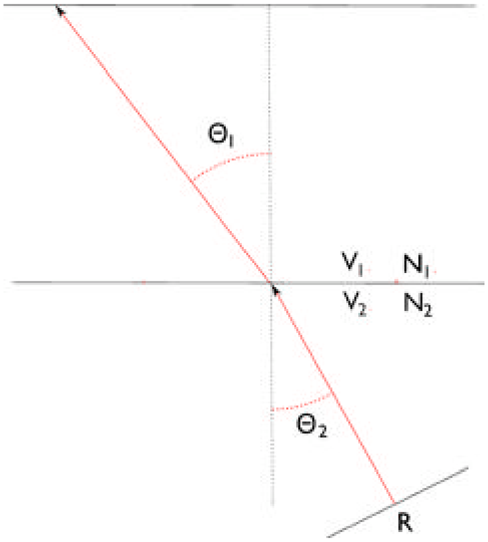

(3-2)

$$\frac{\sin i_1}{\sin i_2} = \frac{V_1}{V_2} = \frac{N_2}{N_1}$$

As long as the velocity depends on depth only, curved rays can be incorporated into the migration process by solving the problem layer-for-layer and then integrating. Since depth is unknown beforehand, it is more consistent to sum over *vertical* time, that is, over the time along a vertical ray. While specific cases can be solved exactly, the general case of arbitrary dependence of velocity on depth requires the two approximations shown Figure 3-17. As will be seen in later sections, the exact traveltime from surface to reflector is given by an infinite series.

Figure 3-17. Curved ray corrections

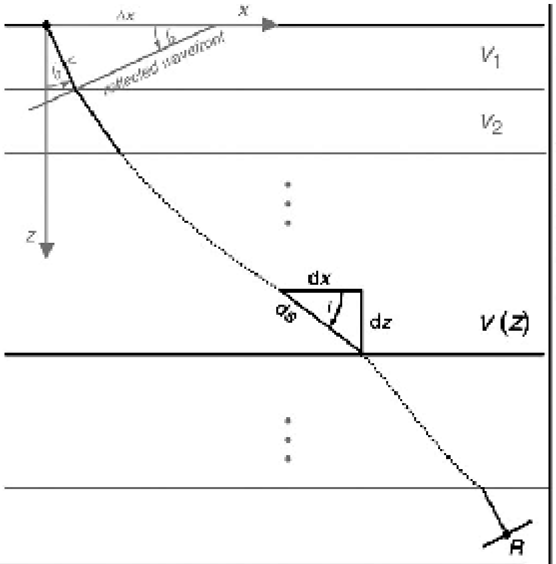

Snell's law: $\frac{\sin i(z)}{v(z)} = -\frac{\Delta t}{\Delta x} = p$

$\sin i = -\frac{\Delta t}{\Delta x}\, v(z)$

$\tau_0 = \frac{2z}{v}$ *(travel time along a vertical ray)*

$v(z) \Rightarrow v(\tau)$ $\quad d\tau = dt\cos i$

$dz = v(\tau)\, d\tau$

$ds = dz/\cos i = v(\tau)\, d\tau/\cos i$

$dx = ds \sin i = v(\tau) d\tau/\cos i \;\; (-v(\tau))\frac{\Delta t}{\Delta x}$

Approximations:

upper limit of integral $t_0/2$ instead of $\tau_0/2$

$1/\cos i \approx 1$

$$x = -\frac{\Delta t}{\Delta x}\int^{\tau_0/2}\frac{1}{\cos i}\, v^2(\tau)\, d\tau + \frac{x_{24}+x_1}{4}$$

$$\approx -\frac{\Delta t}{\Delta x}\int^{t_0/2} v^2(\tau)\, d\tau + \frac{x_{24}+x_1}{4} \qquad \int^{t_0/2} v^2(\tau)\, d\tau = \overline{v^2}\, t_0/2$$

Equation (2)

Thus, the upward traveling wave refracts based on its emergence angle, i, in the layer just above it. When it finally reaches the surface with an emergence angle of i_0, it has traversed the path indicated in Figure 3-17. The formulas integrating $v(\tau)$ over τ, provide the necessary estimate of x. The curved ray formula for x is given by Equation 3-3, where $\bar{v}$, the well known root-mean-square (RMS) velocity, is given by Equation 3-4.

(3-3)
$$x = \frac{\Delta t}{\Delta x}\frac{t_0}{2}\bar{v}^2 - \frac{x_{24}+x_1}{4}$$

(3-4)
$$\bar{v} = \sqrt{\frac{2}{t_0}\int^{\frac{t_0}{2}} v^2(\tau)\, d\tau}$$

Equation 3-3 is important because it tells us how to do an approximate migration when the velocity varies vertically and when rays are allowed to bend or refract. It also provides the mathematical basis for a machine doing the complex migration calculations.

Figure 3-18 shows how the migration formulas in Figure 3-17 can be used, in principle, to construct a machine for performing the migration for a given $\frac{\Delta t}{\Delta x}$ and an average squared velocity given by Equation 3-5.

(3-5)
$$\bar{v}^2 = \frac{2}{t_0}\int^{\frac{t_0}{2}} v^2(\tau)\, d\tau$$

Figure 3-18. Principle for a analog device for event migration.

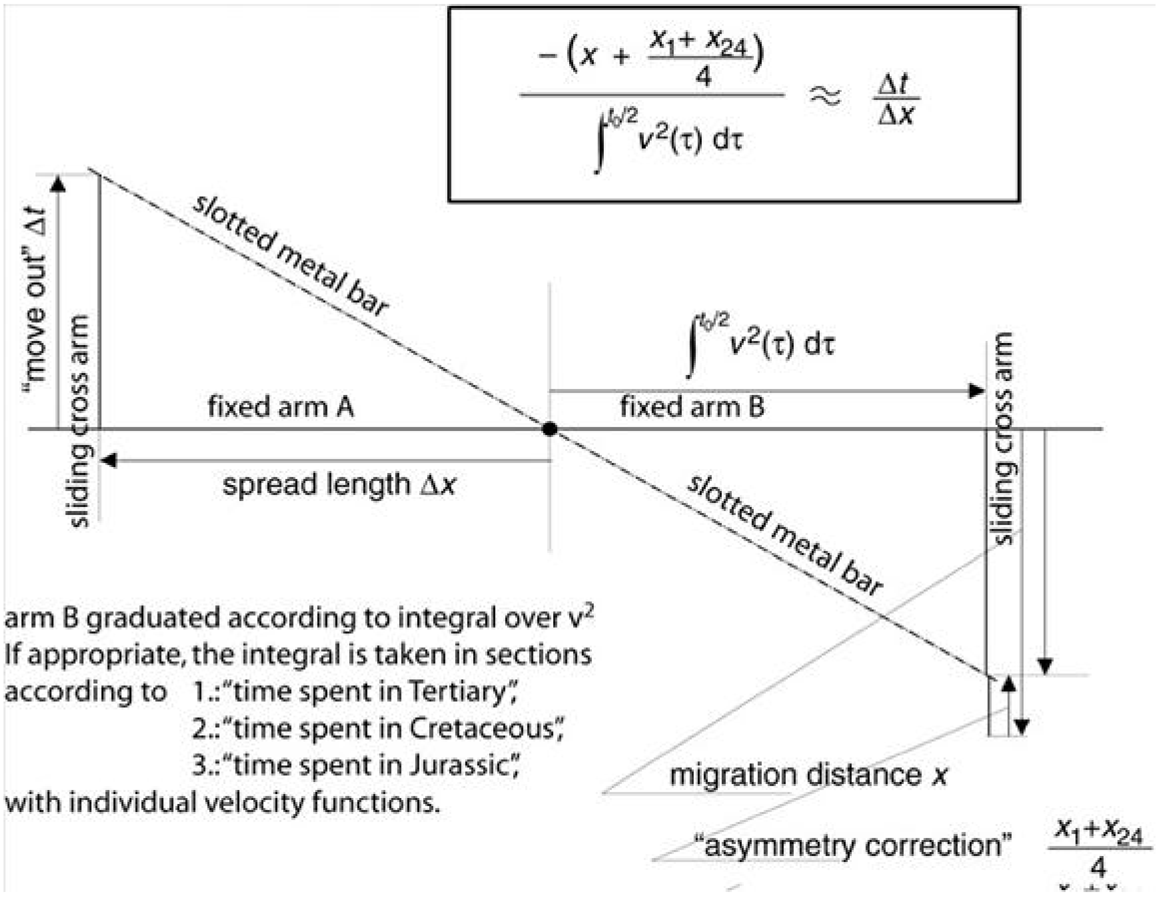

For a given $\frac{x_1+x_{24}}{4}$, the input values for Δt and Δx are input on the left and the migration distance is read off the sliding cross arm on the right. The different parts of this relation are assigned to corresponding sides of two similar triangles.

Figure 3-19 should clarify these comments. Since most reflections were visible on all 24 traces, the Δx setting and the $\bar{v}^2$ setting remains generally constant, at least during the calculation for a single shot record. Since lateral velocity variation was considered to be small, $\bar{v}^2$ also did not change appreciably. What did change was Δt. This change resulted in a *swing* of the machine's arm and consequently devices like that in Figure 3-19 became know as *Swing Arms*. Figure 3-20, from A. W. Musgrave's dissertation at the Colorado School of Mines, shows a real migration machine of the type described figuratively in Figure 3-19.

Figure 3-19. An early migration machine design.

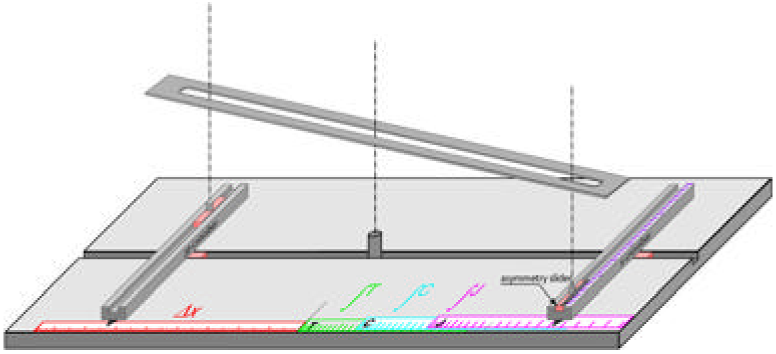

Figure 3-20. A. W. Musgrave's version of a swing arm migration machine

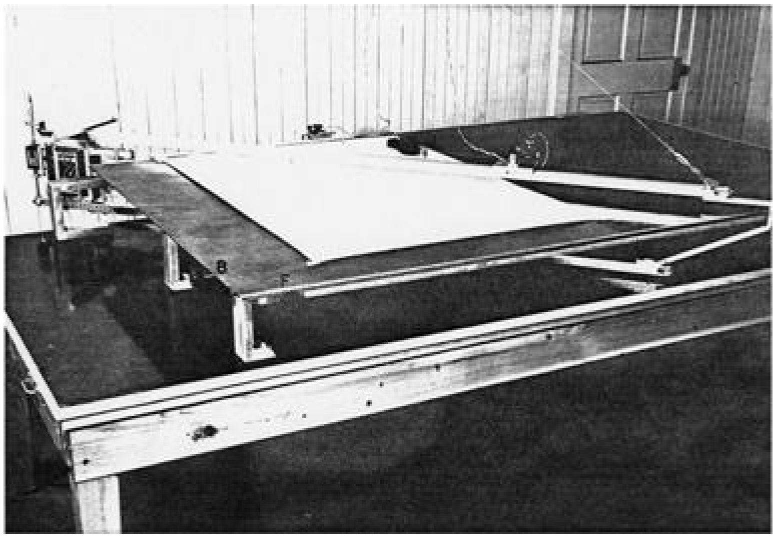

Shot Profile Hand Migration in Three Dimensions

Dipping events are usually from three dimensional reflectors. Figure 3-21 shows one possible approach to figuring out the 3D nature of reflections from dipping events by recording into orthogonal receivers. The idea is to measure and use apparent dips in crossline and inline directions as we did in Figure 3-6 to estimate the distance and direction of the migrated position from the current one.

Figure 3-21. Using a "tee" to detect dip in three dimensions.

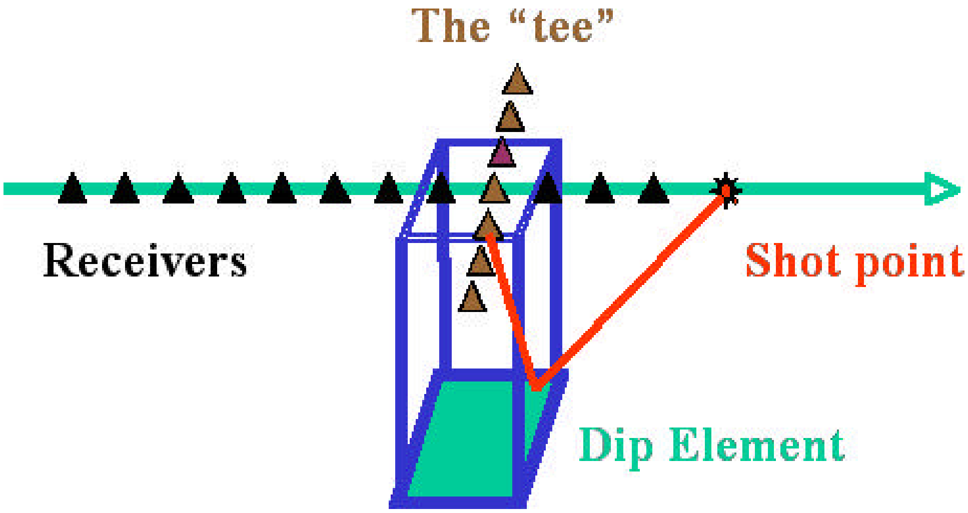

Figure 3-22 shows two late 1940's vintage Amerada Petroleum seismic records showing a "single-end shot record" and what they called a "tee" record for determining the parameters for the calculations described in previous figures. The right-hand side of each record is the single ender while the left-hand side represents the "tee". This kind of cross-spread shooting foreshadowed acquisition of seismic data using orthogonal shot and receiver lines.

Figure 3-22. A "tee" on the left and a single-ended spread on the right in both panels. The "tee" was a string of receivers orthogonal to the direction of the shot line.

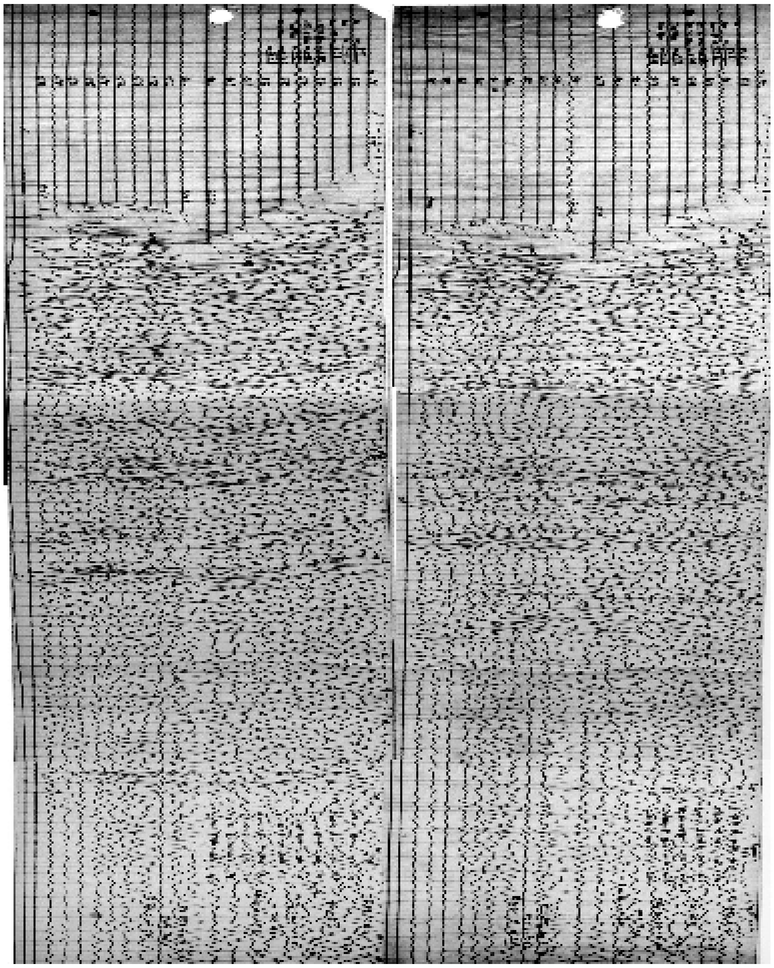

Figure 3-23 shows the simple mathematics of locating the source of the reflected event when there is dip in the x and y directions. This is a 1940's vintage description of how Amerada Petroleum's scientists approached the problem. This kind of solution was considered a top-secret technology in all oil companies of the day.

Figure 3-23. Amerada Petroleum's solution to using the "tee" to resolve 3D dip.

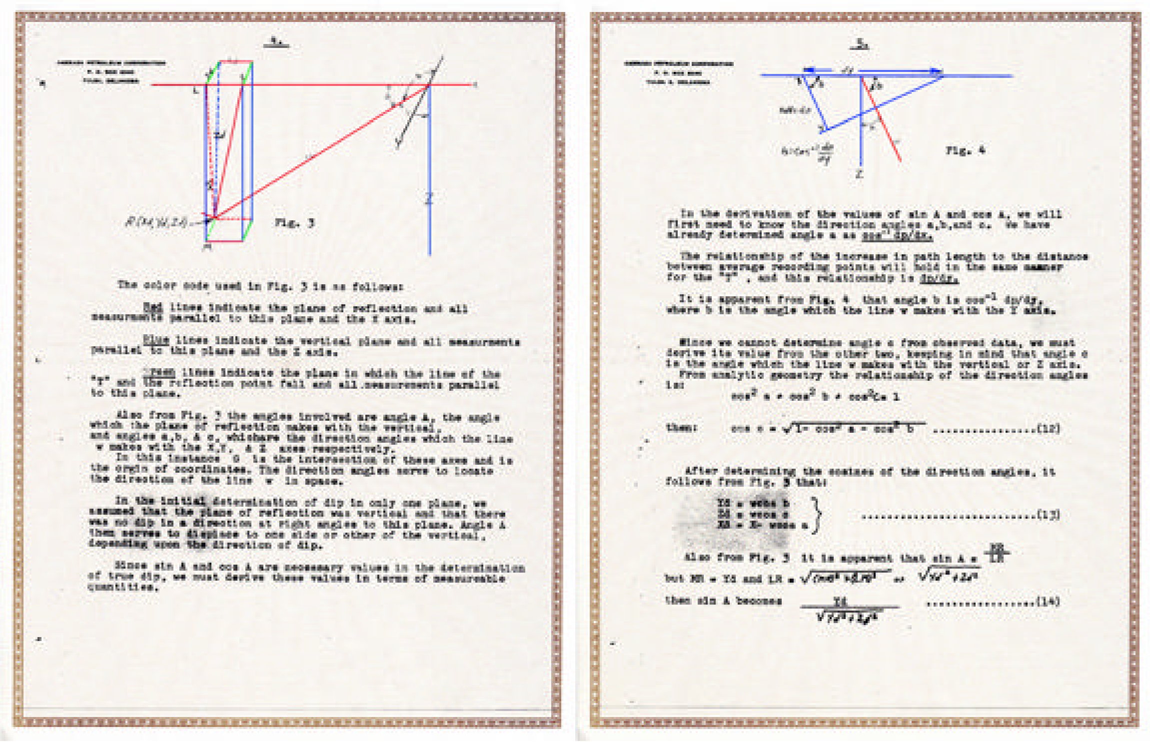

Fig. 3

The color code used in Fig. 3 is as follows:

Red lines indicate the plane of reflection and all measurements parallel to this plane and the Z axis.

Blue lines indicate the vertical plane and all measurements parallel to this plane and the Z axis.

Green lines indicate the plane in which the line of the "T" and the reflection point fall and all measurements parallel to this plane.

Also from Fig. 3 the angles involved are angle A, the angle which the plane of reflection makes with the vertical, and angles a,b, & c, whichare the direction angles which the line w makes with the X,Y, & Z axes respectively.
In this instance O is the intersection of these axes and is the orgin of coordinates. The direction angles serve to locate the direction of the line w in space.

In the initial determination of dip in only one plane, we assumed that the plane of reflection was vertical and that there was no dip in a direction at right angles to this plane. Angle A then serves to displace to one side or other of the vertical, depending upon the direction of dip.

Since sin A and cos A are necessary values in the determination of true dip, we must derive these values in terms of measureable quantities.

$b = \cos^{-1}\frac{dp}{dy}$

Fig. 4

In the derivation of the values of sin A and cos A, we will first need to know the direction angles a,b,and c. We have already determined angle a as $\cos^{-1}$ dp/dx.

The relationship of the increase in path length to the distance between average recording points will hold in the same manner for the "T", and this relationship is dp/dy.

It is apparent from Fig. 4 that angle b is $\cos^{-1}$ dp/dy, where b is the angle which the line w makes with the Y axis.

Since we cannot determine angle c from observed data, we must derive its value from the other two, keeping in mind that angle c is the angle which the line w makes with the vertical or Z axis.
From analytic geometry the relationship of the direction angles is:

$$\cos^2 a + \cos^2 b + \cos^2 c = 1$$

then: $$\cos c = \sqrt{1 - \cos^2 a - \cos^2 b} \quad \ldots\ldots\ldots\ldots(12)$$

After determining the cosines of the direction angles, it follows from Fig. 3 that:

$$\left.\begin{array}{l} Yd = w\cos b \\ Zd = w\cos c \\ Xd = X - w\cos a \end{array}\right\} \quad \ldots\ldots\ldots\ldots(13)$$

Also from Fig. 3 it is apparent that $\sin A = \frac{NR}{LR}$

but $NR = Yd$ and $LR = \sqrt{(mn)^2 + (LM)^2}$ or $\sqrt{Yd^2 + Zd^2}$

then sin A becomes $$\frac{Yd}{\sqrt{Yd^2 + Zd^2}} \quad \ldots\ldots\ldots\ldots(14)$$

Remarks about Migration

Much of what has been discussed so far is what we might call early shot-by-shot migration. Early practitioners of the imaging art were forced to use what they had. They did not have access to modern computers, so sorting data into any other order was impossible because it had not been recorded, impossible because the technology of the day was not capable of doing it, or impossible because it was just too difficult and expensive to consider. There wasn't any way to estimate velocities from recorded data, so shot-by-shot event imaging was the only practical approach.

Without redundancy, velocity information was obtained only by trial and error. If, when tested, a given $v(z)$ was shown to be in error, a new $v(z)$ was selected and used to produce a new stick image. This process was repeated until the result was considered geologically reasonable. This meant that a different flat Earth, vertically varying velocity was being used for each new geologic setting, even if the new location was close to the previous one. It also meant that a large number of different velocity functions might have to be tried before a suitable one was found.

The basic steps in historical *shot-by-shot imaging* are summarized in the following list:

1. Estimate little dip elements from shot-profile records: Single-ended, split-spreads, and "tees".
2. Calculate the distance from the shot-point to the image point using relatively simple math.
3. Place the image point at the estimated depth or vertical (migrated) time to produce a "stick" image.

From a computational viewpoint, this suggests that more than one set of calculations based on Figure 3-17 might be necessary to produce an accurate stick image of any given horizon of interest.

Redundant Data

When multi-fold acquisition consisted mostly of 2D data, receivers were laid out on either side of a centrally placed source. Figure 3-24 shows that this split-spread shooting resulted in redundant data that can be sorted in a variety of ensembles or gathers. In this figure, we see common or fixed-offset, common-receiver, and common-mid-point or common-depth-point gathers. Holding the offset fixed produces sections that, when the offset distance is small, look remarkably like zero-offset profiles. Notice that the term *common-depth-point* really has very little to do with a subsurface point. It is exactly equivalent to a surface source-receiver midpoint. This is also true of common-offset data, where the offset is measured at the surface. Moreover, these data are completely described when the source and receiver locations for the given trace are known. All other information can be computed from these locations.

Figure 3-24. Split-spread acquisition geometry.

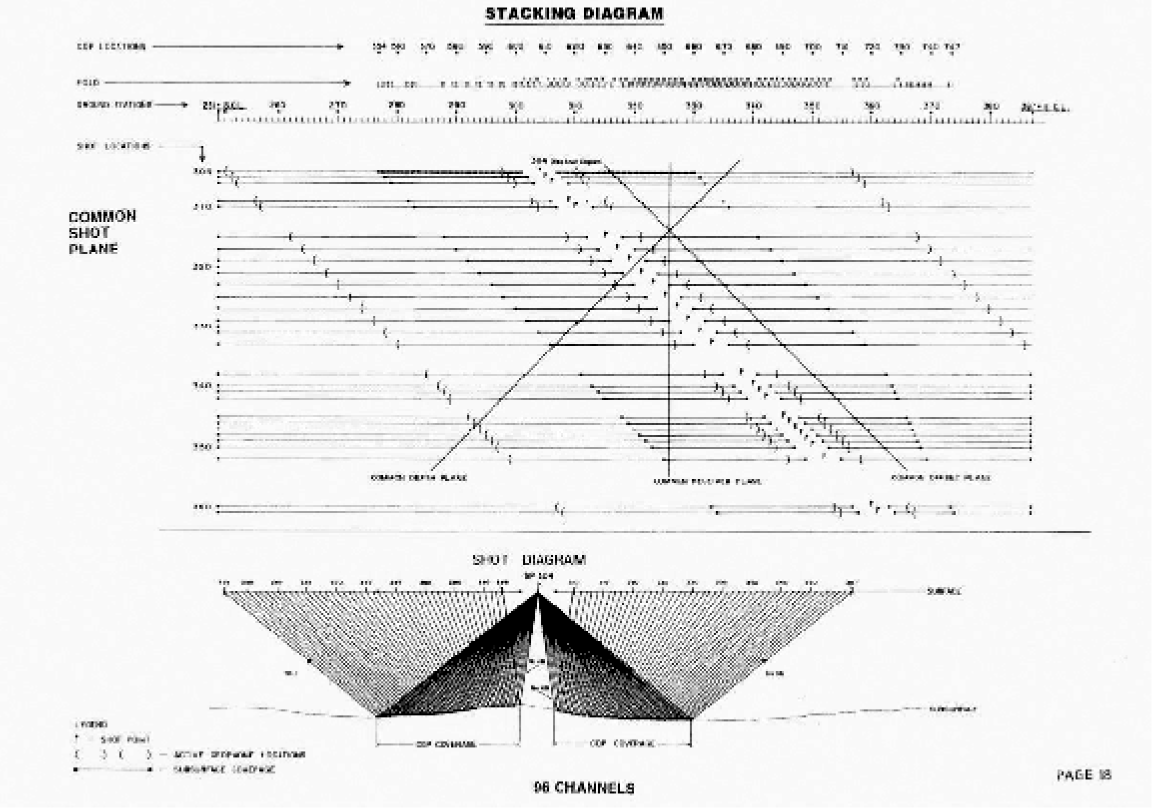

These data, while usually referred to as 2D, actually have three dimensions: source position, receiver position and time. Alternatively, they can be thought of as having common-midpoint, offset, and time as their coordinate system. However we specify the surface data, the resulting volume is three dimensional.

Figure 3-25 shows the split-spread response of a subsurface containing a single reflection point. At the top left, we see the entire response and then, clockwise, the next four figures show a common-offset slice, a common-time slice, a common-angle slice, and a common-midpoint slice. We will see that there are migration algorithms that allow us to migrate data organized in any of these domains.

Figure 3-25. Split-spread point response. The response of a single point to split-spread acquisition.

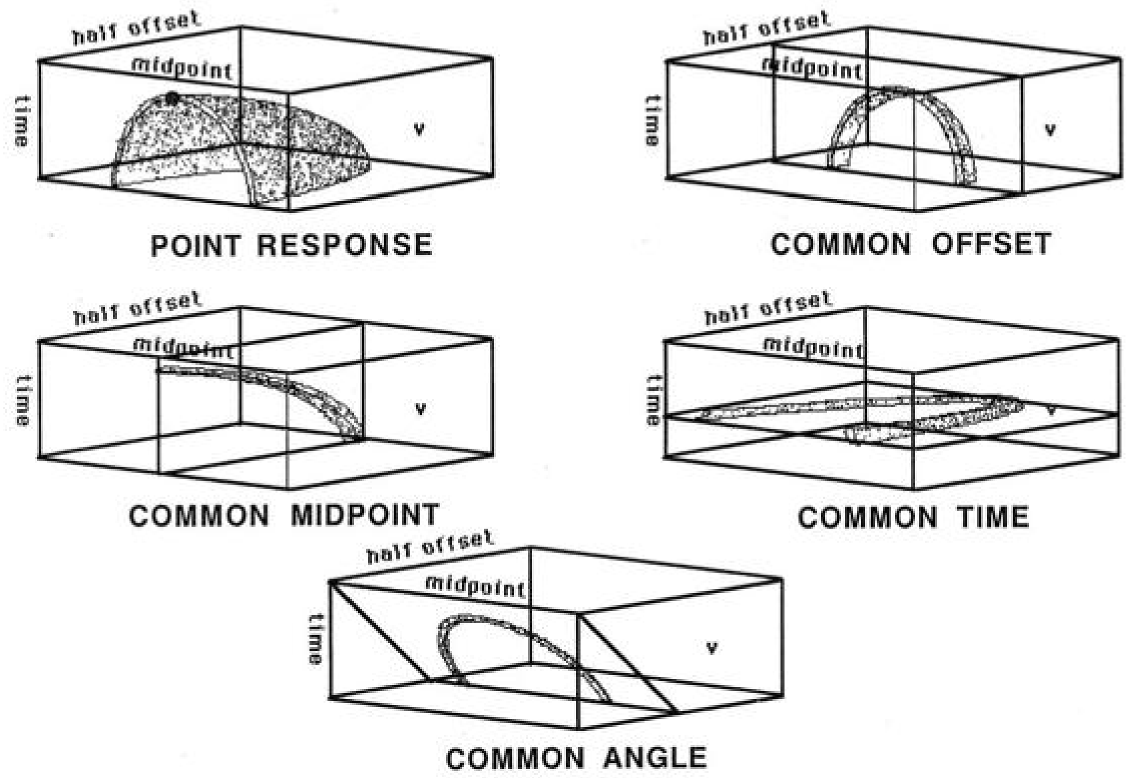

POINT RESPONSE

COMMON OFFSET

COMMON MIDPOINT

COMMON TIME

COMMON ANGLE

Redundant data have many advantages. In the early days, the major advantage arose because they can be sorted into common-mid-point (CMP) order to produce rough estimates of velocity. Although not completely accurate, these velocity estimates were thought to provide the velocity $\bar{v}^2$ so important in the migration approach discussed above. The accuracy of velocities estimated in this way is a function of many things, but the lateral velocity variation due to reflector dip and the velocity variation due angle of propagation can render such estimates almost useless. Only when the Earth is absolutely flat, and there is no variation of velocity with angle of propagation, can such velocity analysis produce accurate values. Nevertheless, the velocities estimated in this way represented a major step forward in improving the accuracy of migrations. Without these estimates, the production of subsurface images probably would not have arrived as early as it did.

Figure 3-26 shows how redundant data provides estimates of velocity. The left side of this figure shows a typical common-midpoint gather. The traces all have the same midpoint, and, if the subsurface reflectors are all flat, the hyperbolic curve in red defines the appropriate velocity to use to correct the data to zero offset time, t_0, and ultimately to produce zero-offset data. Special analog computers were designed and used to estimate $\bar{v}^2(t_0)$ at as many midpoints as possible. Another analog computer stacked the traces in the CMP and the resulting section was migrated using formulas just like those in the previous paragraphs.

Figure 3-26. Flat Earth Society processing to zero offset

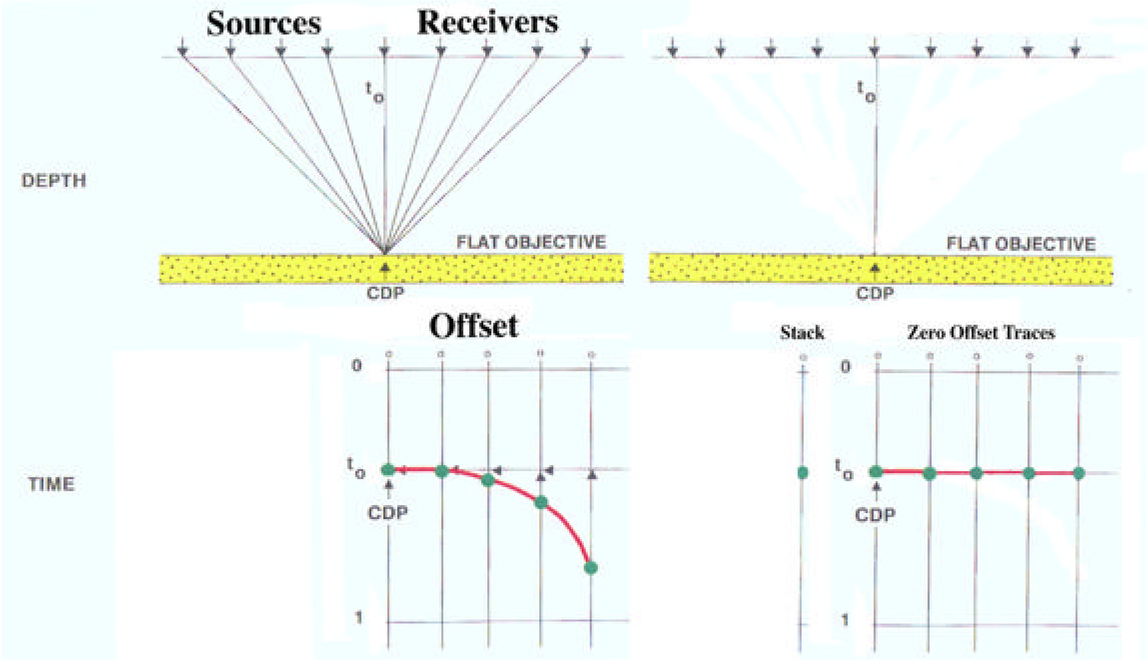

The right hand side of Figure 3-26 shows the application of a dynamic correction known as normal moveout (NMO) to correct the hyperbolic response to a flat one. Part of the definition of NMO from Wikipedia (Wikipedia contributors, “Normal Move Out” Wikipedia, The Free Encyclopedia, Wikipedia link):

> Because the wave must travel along the hypotenuse created between the depth of the event and source-receiver offset, the time delay increases hyperbolically along equally spaced geophones. The hyperbolic distortion must be corrected in order to accurately image the subsurface.

The result of summing the dynamically corrected traces for every CMP is called a *stacked section.*

Swing Arms

This section presents additional information about swing arms, which were mechanical devices enabling you to migrate dip data. See also Curved Rays on page 100 for more information about swing arms.

Isopachs and Isochrons

In view of the comments in the preceding sections, one conclusion becomes quite clear—any apparent reflection on any given trace could have come from any point on an equal traveltime subsurface *isopach*. An equal traveltime isopach is that set of points in the subsurface whose traveltimes from the surface and back (two-way times) are identical. Figure 3-27(a) shows an equal traveltime curve in a constant velocity medium for zero-offset reflections. Clearly, if all we have is a zero-offset trace, we can only infer that the reflection could have come from any point on the equal-traveltime isopach defined by the reflection time.

Figure 3-27(b) provides the simplest mathematics defining an equal traveltime curve. It also shows how the apparent horizon (dotted line) is imaged as the envelope (dark solid line) of a set of equal traveltime curves.

Figure 3-27. Equal traveltime curves in a constant velocity medium.

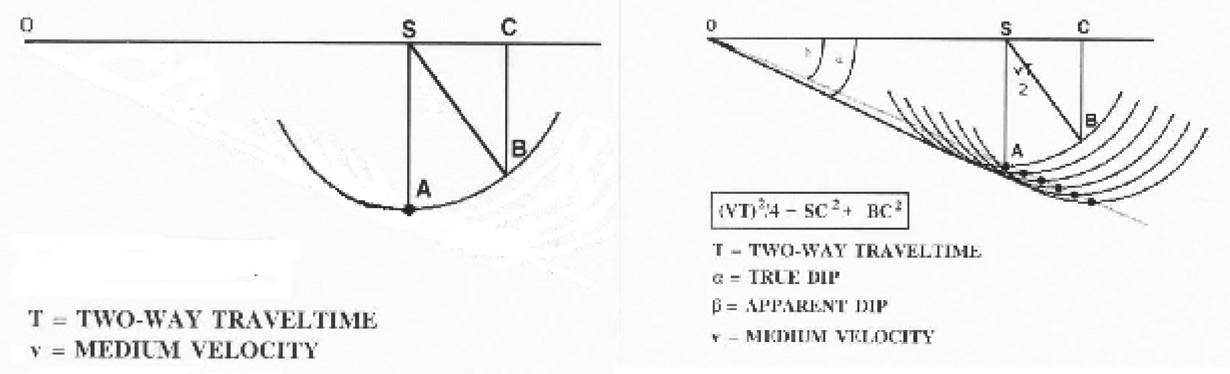

(a). Equal traveltime curves for zero offset data **(b).** Migration with equal traveltime curves

For any given arrival on a recorded seismic trace, all potential locations from which this arrival could have been reflected lie on a circle with the source point as the center and the velocity-time depth as the radius. If we trace out a circular isopach for each source, the envelope of all such isopachs will be the location of the actual reflecting surface. Since the velocity is assumed to be constant, these circular isopachs can also be thought of as isochrons, or curves and surfaces in time rather than depth. Regardless of terminology, a swing-arm built on this principle has a significant advantage over hand plotting each vector to migrate the given dip data. An entire zero-offset stick map could be migrated with a constant velocity without every resorting to any calculations at all. Of course, the constant velocity assumption meant that the results might not be accurate, but they could be redone quickly. A different constant velocity could be used for each surface position to at least make the resulting migrated stick map as close as possible to subsurface truth.

Operators

Figure 3-28 provides the time response on the surface for a single point reflector in the subsurface.

Figure 3-28. Operators and operator migration—Point reflector zero-offset response

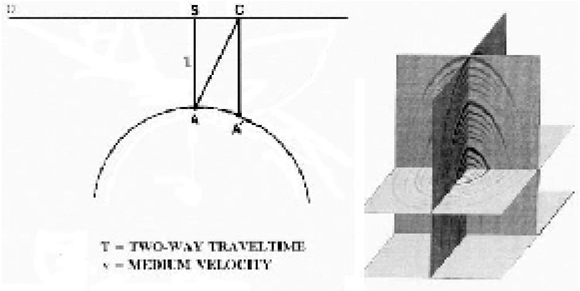

Every time on this time domain curve is the two-way time from the surface source to the point reflector and back to a receiver at exactly the same location as the source. The time recorded at A' below C is actually the time it would take for sound to travel from a source at C to the point reflector below S and back to a receiver at C. As indicated in Figure 3-28 for a constant velocity medium, the set of all such times can be calculated quite easily using Pythagorus' theorem.

$$T = \sqrt{T_0^2 + \frac{(C-S)^2}{v}} \tag{3-6}$$

In a more complex velocity medium, the curve would not be a circle, but would still represent the zero-offset reflection times from the point reflector. Zero offset responses are quite easy to calculate, and raytrace modeling is fully capable of calculating such responses in virtually any medium.

The operator approach to migration computes an operator curve, intersects it with each input trace, selects the amplitude at the intersection time, and then adds it to the image point or output location on or near the top of a downward facing frown. In actuality, this is completely equivalent to the previous diffraction-based approach. They both produce the same result, but this one is a bit more difficult to understand. Figure 3-29 shows an amplitude at A being moved to the top of the zero-offset response curve and added to the reflection point location at B. In general, all the amplitudes that intersect the operator would be summed into the top of this curve at point B. However, the only non-zero amplitude point that we can see is at A. As the process continues, each and every point on the apparent or unmigrated reflector is moved to the top of the associated zero-offset response curve and added to the appropriate spot on the migrated image represented by the solid line in Figure 3-29.

Figure 3-29. Operators and operator migration—Zero-offset response or operator migration

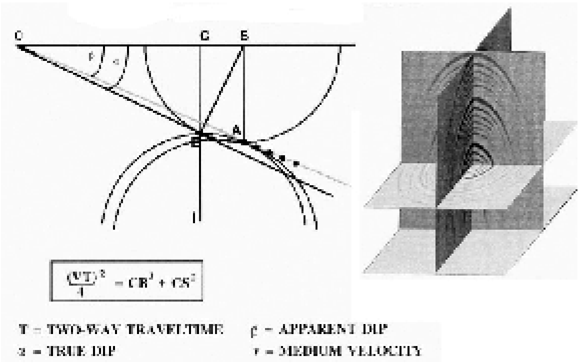

The three-dimensional figure on the right illustrates all the amplitudes from surrounding traces that contribute to the trace in the middle. These frowns are called operators, but they are really the modeled response of a point reflector at some subsurface location. The important thing is the process and not the shape of the zero-offset response.

This approach to migration is somewhat more difficult to understand than the *spray* approach of the previous section. Why it works should become much clearer in the chapter on seismic modeling. However, one thing should be clear, it is based on modeling a point reflector and not on the possible locations from where the reflector might have come.

Non-Zero Offsets

Figure 3-30 shows the ellipse representing the set of points whose traveltimes from a source at S to a receiver at R are identical. Producing this kind of curve in variable velocity mediums became practical with the advent of digital computers. Migration of fixed-offset data follows the same principles at shown in the zero offset case shown in the bottom image in Figure 3-27. There is, of course, a corresponding non-zero-offset operator-based approach to migration. Raytracing is used to compute the traveltime from any given source to a reflection point, then from the reflection point back to the receiver on the surface. Operator migration then proceeds in the same manner as it did in Figure 3-28.

Figure 3-30. Fixed offset equal-travel-time curves.

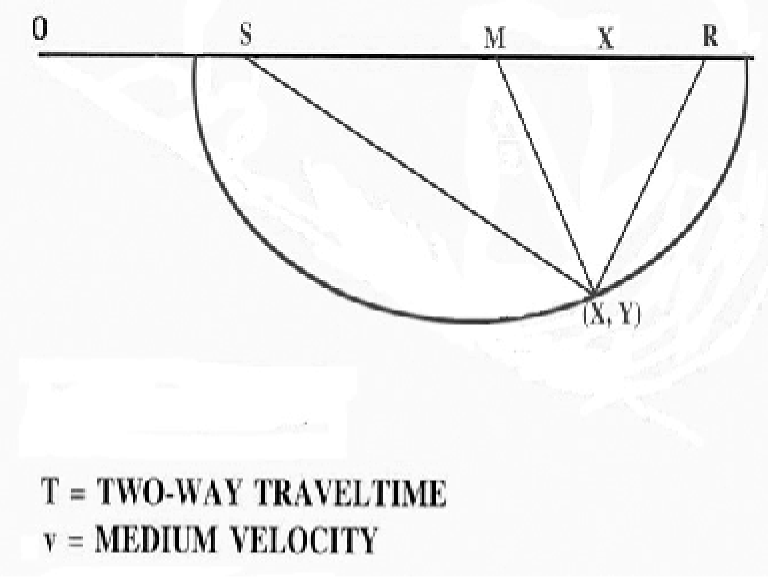

It is clear from Figures 3-27 through 3-30 that if we wish to use the concepts involved in the most general possible case, we must compute traveltimes from any given source to a potential reflection point and then back to a fixed receiver. Just prior to the advent of digital computers and to some extent beyond that time, efforts were made to do just that. Analog devices were designed to compute these traveltimes in the form of *wavefront charts*.

The mathematics in Figure 3-31 was used to compute the wavefront charts in Figure 3-32. It is not important to understand the mathematics. What is important is that the formulas provide a method for calculating the two-way traveltimes from any point on the surface to any point in the subsurface of a $v(z)$ medium and back. Today, the traveltimes originally chosen from wavefront charts are easily and very repetitively computed via raytracing. What is also important is that this approach was known and used in the mid 1950's for performing complex migrated stick figure reconstruction of picked seismic arrivals.

Figure 3-31. Wavefront chart mathematics

$$x(i) = \frac{2z_0^{(2)}}{\sin^2 i_0}\int_{i_0}^{i}\sin^2\chi\, d\chi = \frac{z_0^{(2)}}{2\sin^2 i_0}\left(2i - 2i_0 - \sin 2i - \sin 2i_0\right),$$

$$z(i) = z_0^{(2)}\left(\left(\frac{\sin i}{\sin i_0}\right)^2 - 1\right) = \frac{z_0^{(2)}}{2\sin^2 i_0}\left(1 - \cos 2i - \cos 2i_0\right),$$

$$t(i) = \frac{2z_0^{(2)}}{v_0 \sin i_0}\int_{i_0}^{i}\chi\, d\chi = \frac{i - i_0}{\sin i_0}\tau_0 .$$

These are the equation of a right cycloid generated by a circle with

$$R = \frac{1}{2}\frac{z_0}{\sin^2 i_0} = \frac{1}{2}\frac{z}{\sin^2 i}$$

The wave front charts in Figure 3-32 are based on the mathematics of Figure 3-31. The charts represent the velocity functions in Equation 3-7, where $n = 0$ is constant velocity, $n = 1$ is standard chart (constant velocity gradient, rays are circles, fronts are spheres), and $n = 2$, which is more realistic, but in the pre-computer days, difficult to generate.

$$\left(\frac{v}{v_0}\right)^n = \frac{z + z_0}{z_0} \qquad (3\text{-}7)$$

Figure 3-32. Wavefront charts

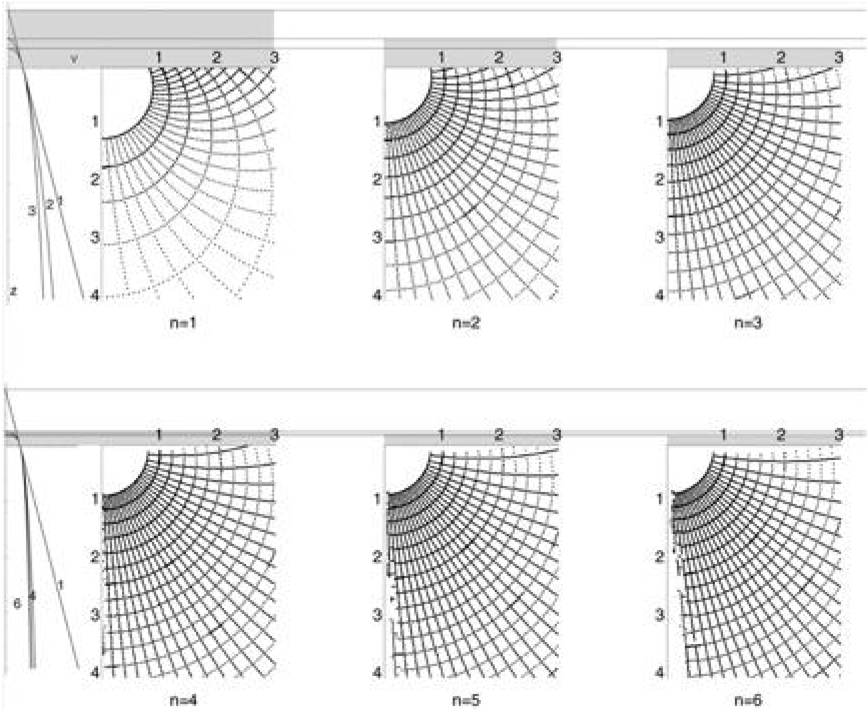

It may not be clear from these figures, but the construction of any given wavefront chart is based on the utilization of circles to generate rays. This should not be too surprising since, for any given constant velocity, the point response is defined by the equation of a circle.

Once the concept, as shown in Figure 3-33, is understood, it is quite reasonable to construct a mechanical device to both calculate the wavefronts and also produce stick figure images. By the late 1950's and into the early 1960's, machines were constructed to perform migration based on the wavefront charts in Figure 3-32. Thus, Figure 3-33 is a geometrical picture of the mechanical basis for a machine such as A. W. Musgrave's wavefront charting machine shown in Figure 3-34. Note the charts on the surface. This machine is actually an analog device for raytracing. I don't know about you, but this looks like a printing press to me. Unfortunately, no such machine appears to have survived.

Figure 3-33. The geometric basis for A. W. Musgrave's migration machine

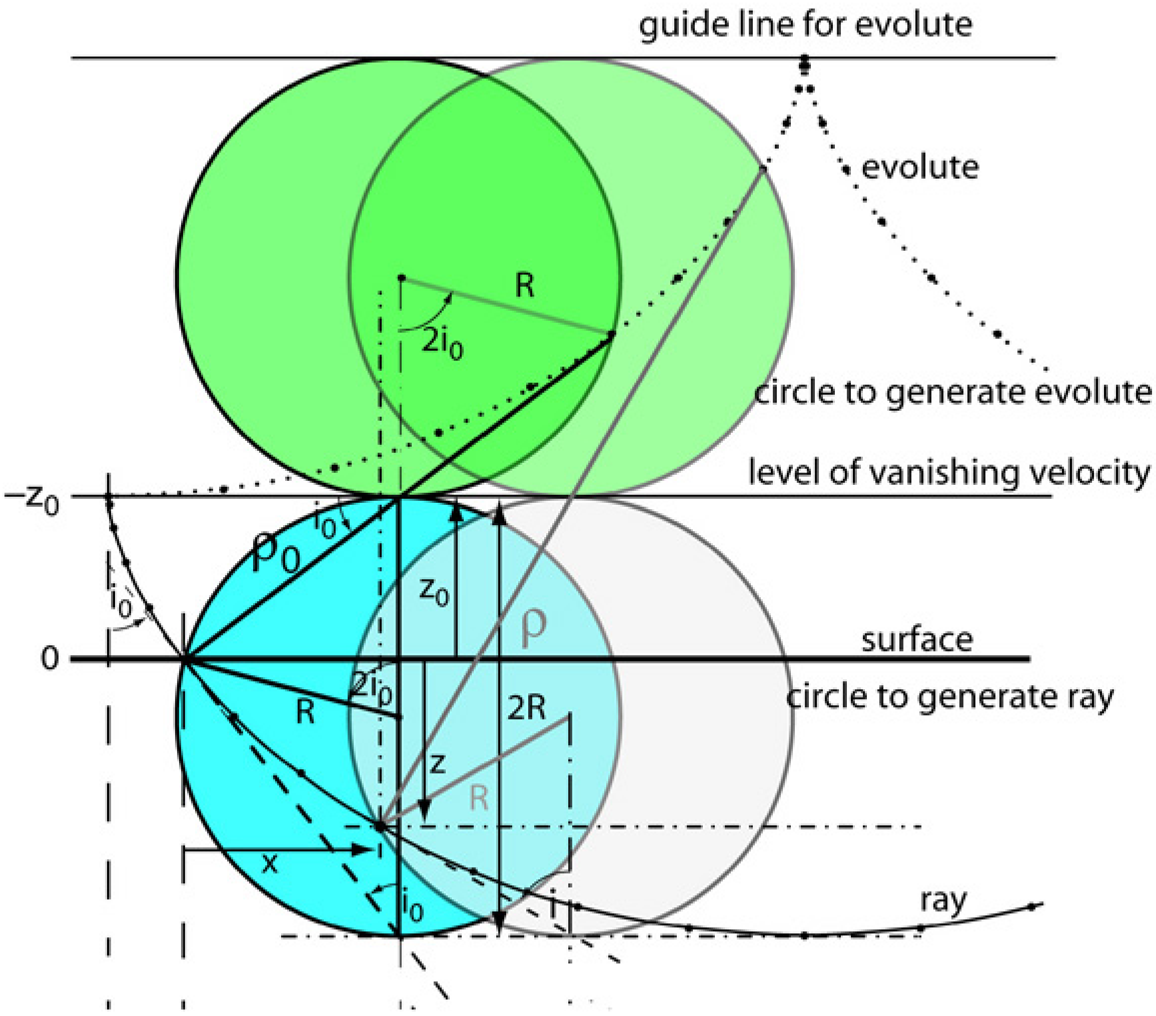

Figure 3-34. A. W. Musgrave's migration machine

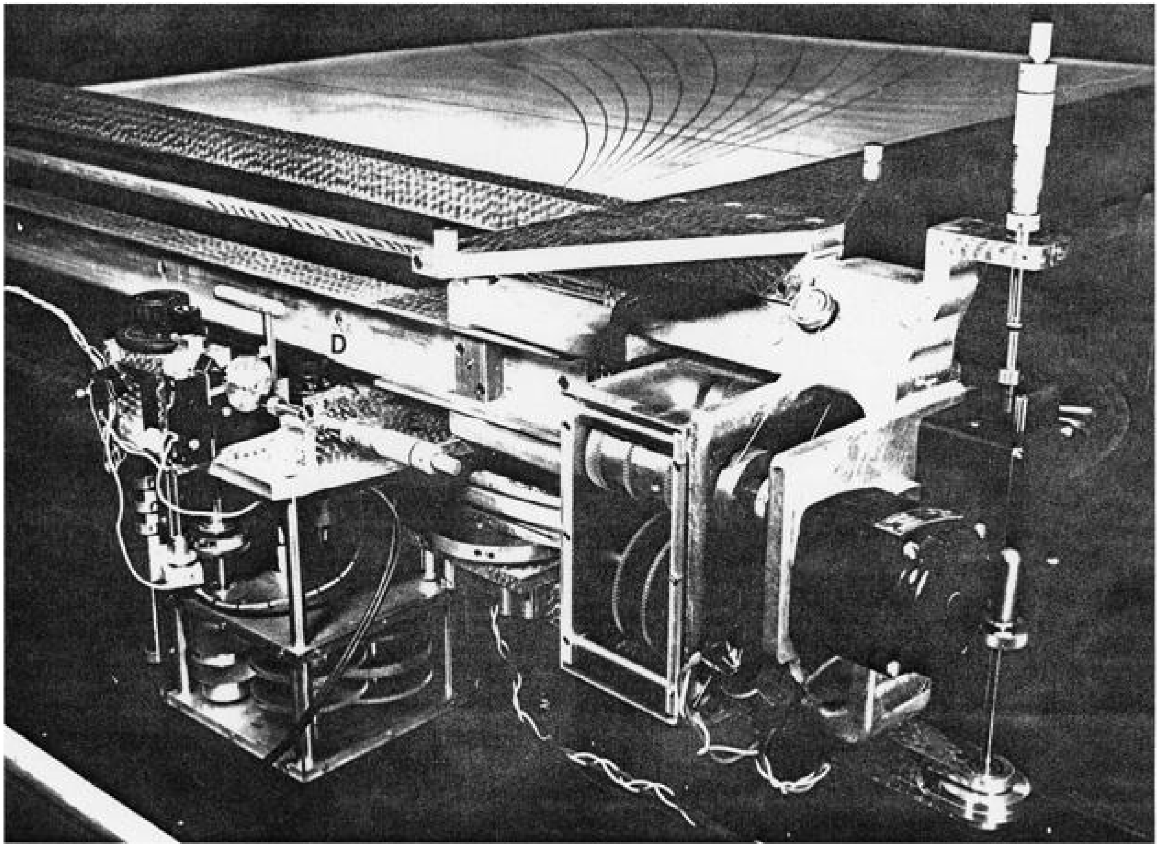

It is important to note that in the real world, because the sources and receivers are at discrete locations, we must consider our measured seismic data to be digital in character. Since modern data is also digital in time, reflection seismic processing today is purely digital. Since the wavenumbers of propagating plane waves carry information about the angle of propagation, this suggests that there will be some issues with regard to the aliasing of dipping subsurface reflectors. The impact of aliasing on our ability to image subsurface events will be discussed in subsequent sections.

Stacking and DMO

The primary purpose of this section is to provide a simple understanding of why certain parts of early digital processing techniques did not image all of the Earth's structures. This, in effect, is an interpretation issue. We will see that what might be considered easily imaged events are sometimes totally invisible in the seismic record. In many such cases, parts of the subsurface structure may be invisible simply because we have not applied the most accurate available technique to image it. In other cases, its absence may be due to improper noise suppression techniques applied during the preprocessing steps. Whatever the cause, the idea is always to be able to understand what approach produces the best image.

What is Stacking and DMO?

As we will see, migration can be split into four conceptual pieces. As a rule of thumb, these four pieces will help us understand what migration is and how it naturally completes the imaging process.

1. The first piece is called *normal moveout* (NMO). When the world is flat, NMO corrects for the fact that the source and receiver are not coincident, but it cannot do so when the reflections come from dipping horizons.
2. The second piece of migration corrects for dip. Historically, this second piece was called *dip-moveout* (DMO), but, in the cases of interest here, it happens within the migration methodology itself.
3. The third migration piece shifts events on each moveout-corrected offset to its true subsurface position.
4. The fourth and final piece sums (stacks) all the redundant traces into the final image.

When the Earth's velocity has very little lateral variation, these four operations can be split apart and applied in any desired order. The most familiar order is NMO, DMO, stack, and finally migration. However, when the velocity is almost constant, it is quite possible to use the order DMO, migration, NMO, and stack. Full prestack migration can be thought to have the order DMO, NMO, imaging, and stack, but in reality the sequence DMO, NMO, and imaging is usually done in one giant process.

Initial attempts at subsurface imaging forced the geophysicist to join the Flat Earth Society. For a constant velocity medium, Figure 3-35 shows that Greek mathematics can be used to provide the total travel time, t, from a surface source to a flat subsurface reflector and back to a surface receiver. This is done in terms of the two-way vertical travel time, t_0, from the midpoint, M, to the reflector and back to the surface. Since neither the velocity, v, nor the vertical or “zero-offset” traveltime is usually available directly, redundant source and receiver configurations must be used to estimate the traveltimes. For most acquisition geometries, redundancy is usually sufficient to simultaneously estimate both t_0 and v.

Figure 3-35. Constant velocity NMO.

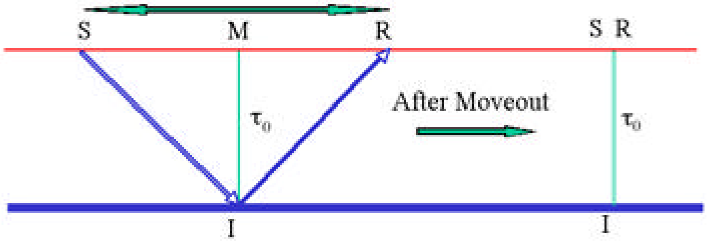

$$\boxed{v^2\tau^2 = SI^2 = Z^2 + (S-M)^2 = v^2\tau_0^2 + \frac{h^2}{4}}$$

$$\boxed{\tau^2 = \tau_0^2 + \frac{h^2}{4v^2}}$$

The subsurface image point, I, is usually referred to as the *common-depth-point* (CDP). The common depth point is the halfway point in the travel of a wave from a source to a flat-lying reflector to a receiver. When we know the velocity, the arrival at time t and offset h can be moved to time t_0. This process is usually called *normal moveout correction* (NMO). After NMO, all traces with a common-midpoint are summed to remove the redundancy and produce a zero-offset trace.

However, for our purposes, the important thing is that this vertical time shift is the first step in formulating a prestack approach to imaging. The shift corrects to the arrival time consistent with coincident sources and receivers. After NMO, the result is as though the source, S, and receiver, R, were located at the midpoint, M.

The traces in the CDP gather of Figure 3-36 all have the same midpoint. When the subsurface reflectors are all flat, the hyperbolic curve in red defines the appropriate velocity to use to correct the data to zero offset time t_0. A modern computer easily fits the data and provides the graphics to estimate both the vertical traveltime and the velocity. The vertical traveltime, t_0, in this figure is extremely important. Keep this in mind as the book continues.

Figure 3-36. Typical midpoint gather.

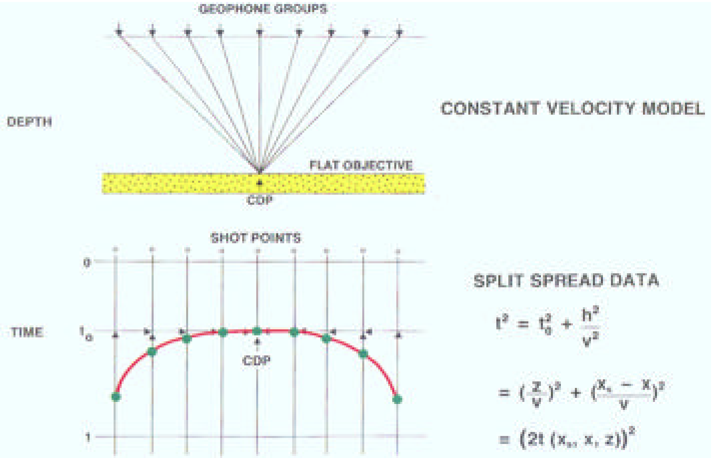

The shots in Figure 3-37 are from the pyramid model in Figure 3-38.

Figure 3-37. Shots 1-24 from the Pyramid model

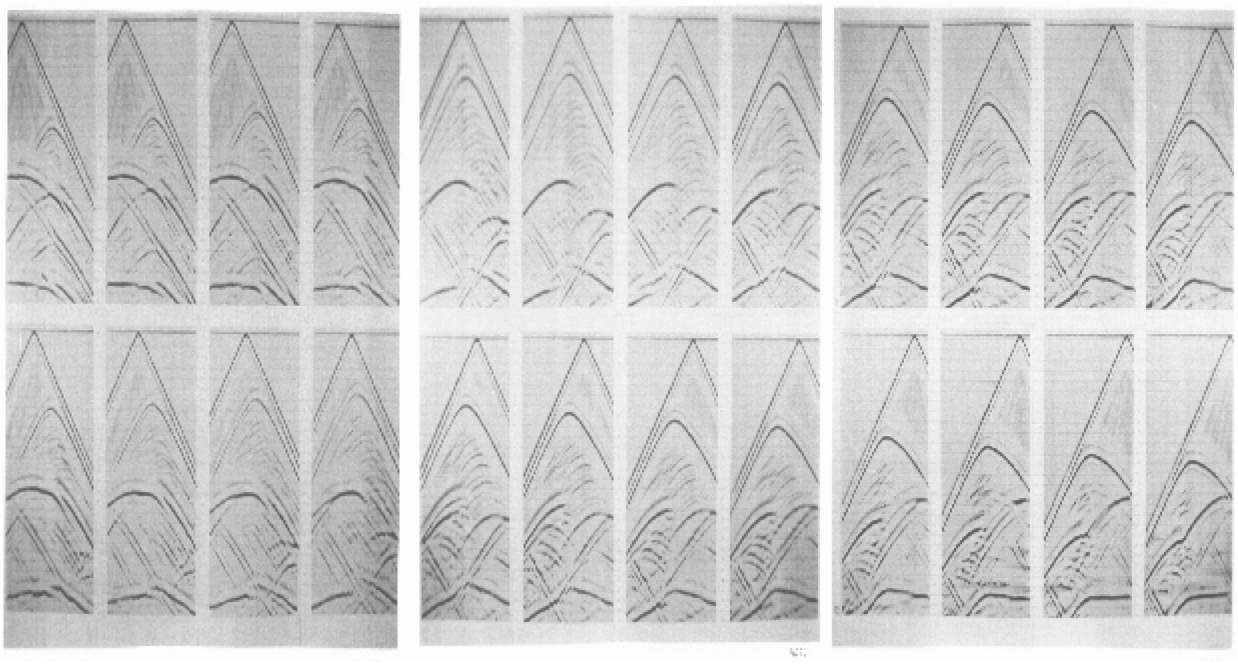

Figure 3-38. The Pyramid Model

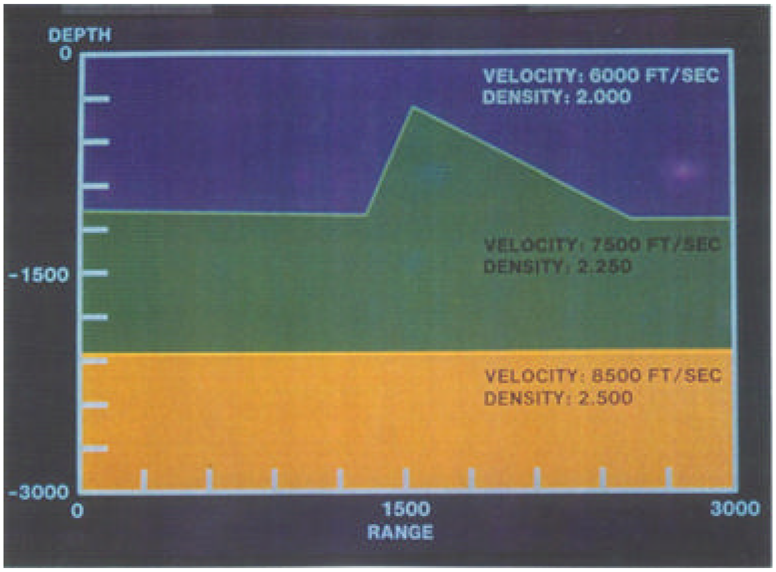

Figure 3-39 is a stack of the common-midpoint ordered data in Figure 3-37. NMO was performed using the root-mean-square velocity from the model used to generate the data. The "noise" in this data set is representative of a poor implementation of the approximations to the differential equation used to model the data. This kind of noise is related either to the fact that the differences have not been approximated well, or because damping at the boundaries is poor.

Figure 3-39. The stack of Shots 1-24 from Figure 3-37.

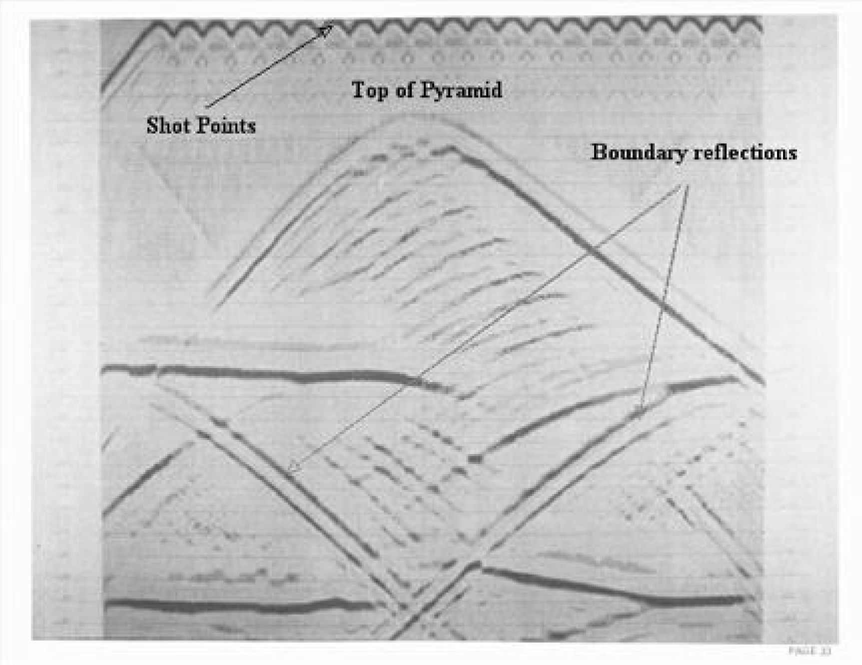

Figure 3-40 shows how dip affects arrival times as a function of half-offset.

Figure 3-40. Moveout for a dipping reflector.

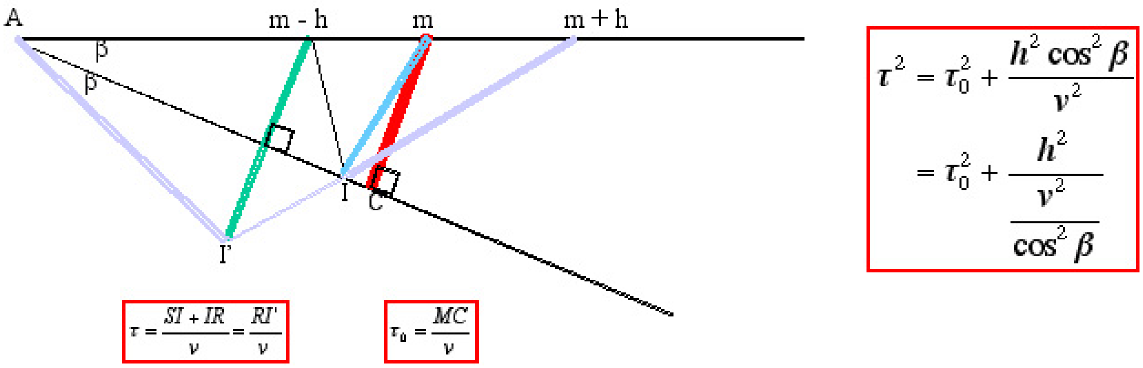

To relate the traveltime from source at $m - h$ (S) to the image point, I, and back to the receiver at $m + h$ (R), note that in Figure 3-40, the length of the path from S to I and then to R is the same as the length from R to I'. Using the law of cosines, we have Equation 3-8.

(3-8)
$$\begin{aligned}(RI')^2 &= (AI')^2 + (AR)^2 - 2(AI')(AR)\cos 2\beta \\ &= (m-h-A)^2 + (m+h-A)^2 - 2(m-h-A)(m+h-A)\cos 2\beta \\ &= 2(m-A)^2 + 2h^2 - 2(m-A)^2\cos 2\beta + 2h^2\cos 2\beta \\ &= 2(m-A)^2(1-\cos 2\beta) + 2h^2(1+\cos 2\beta) \\ &= 4(m-A)^2\sin^2\beta + 4h^2\cos^2\beta\end{aligned}$$

To get the time over the path from R to I', divide each side of Equation 3-8 by v^2, as shown in Equation 3-9.

(3-9)
$$\frac{(RI')^2}{v^2} = \frac{4(m-A)^2\sin^2\beta}{v^2} + \frac{4h^2\cos^2\beta}{v^2}$$

Since the vertical traveltime is given by Equation 3-10, we get the final equation, Equation 3-11.

(3-10)
$$\tau_0 = \frac{MC}{v} = \frac{(m-A)\sin\beta}{v}$$

(3-11)
$$\tau^2 = \tau_0^2 + \frac{h^2\cos^2\beta}{v^2} = \tau_0^2 + \frac{h^2}{\frac{v^2}{\cos^2\beta}}$$

The cosine term in the denominator of Equation 3-11 essentially increases the apparent velocity of the dipping reflector. For example, the apparent velocity of a bed dipping at 60 degrees will be exactly twice that of a flat reflector in the same velocity medium.

Figure 3-41 shows that reflections from a dipping reflector in a constant velocity medium appear to be from a flat reflector with a velocity of $\frac{v}{\cos\beta}$. The blue hyperbola is what actually defines the dipping event. The red curve is the hyperbola from a flat reflector with the same velocity, v.

Figure 3-41. The impact of dip as seen on a common-midpoint gather.

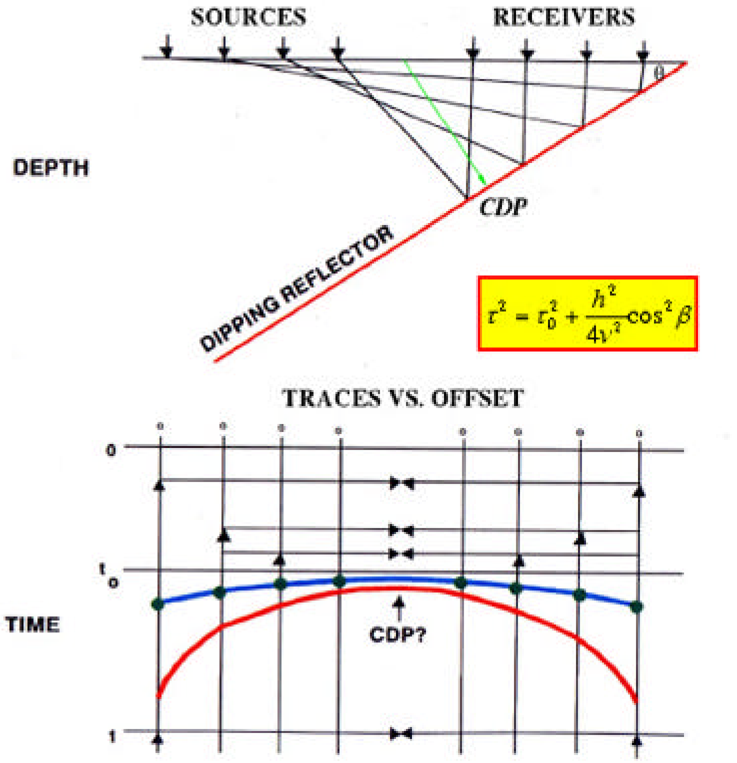

Note that for traces with a fixed midpoint, reflections from the dipping horizon do not correspond to a fixed common-depth-point (CDP) location (the intersection of the green line and the dipping reflector). In fact, the larger the offset between source and receiver, the greater the CDP-reflection point separation. This separation is referred to as *CDP smear*. To correct precisely for CDP smear requires that we prestack migrate the traces, since normal moveout will not work.

Nevertheless, the hyperbolic curve (blue in the figure) can still be corrected and stacked, it just cannot be stacked with the true velocity v, but must be stacked with the normally much faster velocity, $\frac{v}{\cos\beta}$. Thus, if we assume that the CDP smear is small, we could, in principle, stack the data with the faster velocity and produce some kind of representation of the dipping event. One way to do this, and then combine the dipping information with the standard stack, is to NMO with the faster velocity, filter out anything that is not flat, stack and then add the result back to the NMO stack.

Examples

To see how this might work, we will stack the data with velocities of the form $\frac{v}{\cos\beta_i}$ over a uniform range of angles β_i, filter out anything that is not flat on the CDP gathers, and then stack.

Figure 3-42 is an example stack of a two-dimensional Gulf of Mexico data set over an obvious salt structure. The process used to generate this unmigrated image was simply NMO followed by stack. There was no intermediate dip correction or migration.

Figure 3-42. A typical stack of a 2D data set from the Gulf of Mexico. This data was shot sometime in the 1980's.

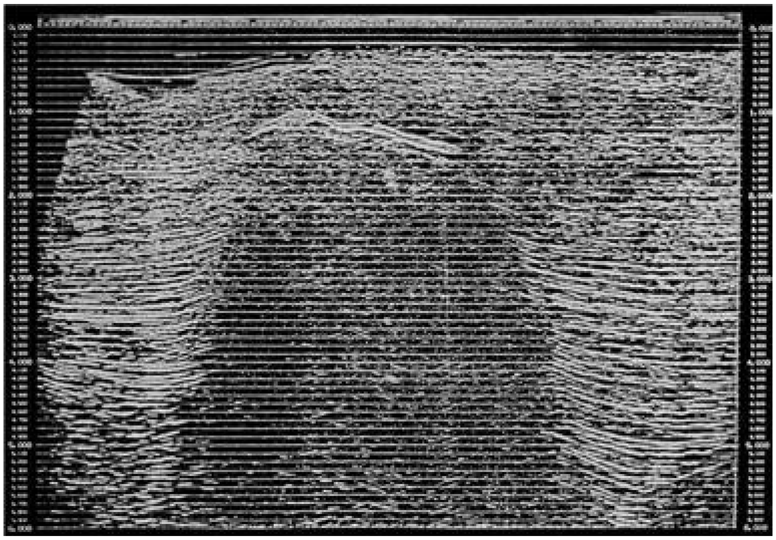

Figure 3-43 is a stack of a Gulf of Mexico salt structure using parameters and filters that attempt to image dip up from 0 to 15 degrees. What we actually did was find a set of velocities that we thought represented the sediment velocities, and then filter out all of the events that were over-corrected by normal moveout. Our best estimate is that the actual dips of the reflections comprising this image are no larger than 35 degrees.

Figure 3-43. Stack of the data in Figure 3-42 using an assumed dip of 7.5 degrees. At the bandwidth of these data the effect is to stack everything up to approximate 15 degrees.

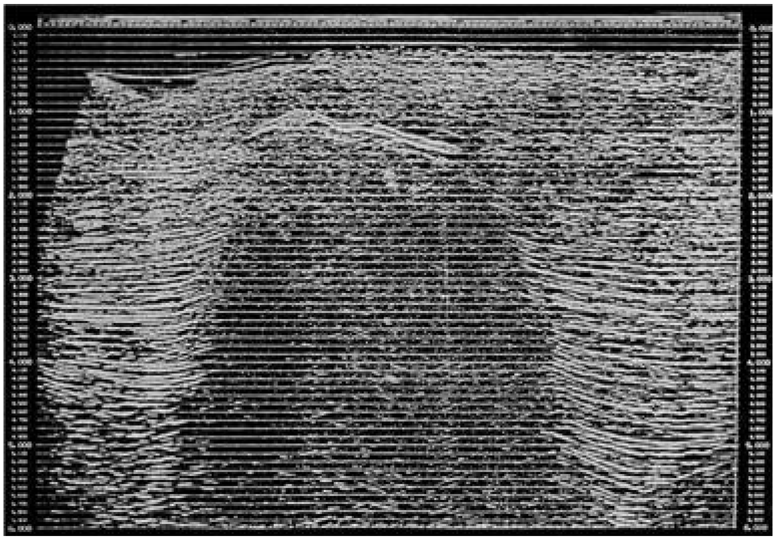

Figure 3-44 is a stack of a the Gulf of Mexico salt structure with parameters chosen to image events from beds with 15 to 30 degree dips. Note that what we are seeing are mostly reflections from beds whose dip is increasing as they approach the salt dome.

Figure 3-44. Stack of the data using an assumed dip of 22.5 degrees. At the bandwidth of these data the effect is to stack everything between 15 and 30 degrees of dip.

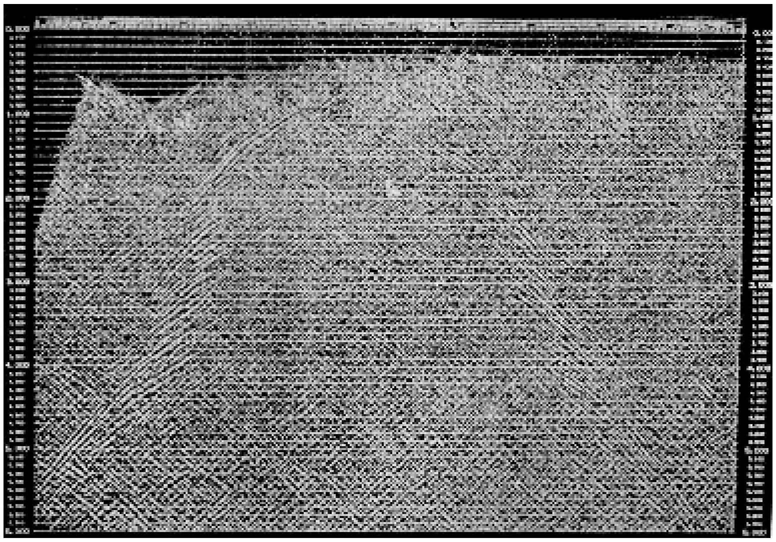

Figure 3-45 shows the stack of data over a Gulf of Mexico salt dome with parameters chosen to image reflections from events with 30 to 45 degree dips. As we increase the angle of the dips we are trying to image, we see that events reflected from more steeply dipping beds begin to appear. Again, this unmigrated image was produced by modifying the normal stacking velocity field to produce an apparent velocity field closely associated with dipping events in the 30 to 35 degree range.

Figure 3-45. Stack of the data using an assumed dip of 37.5 degrees. At the bandwidth of these data the effect is to stack everything between 30 and 45 degrees of dip.

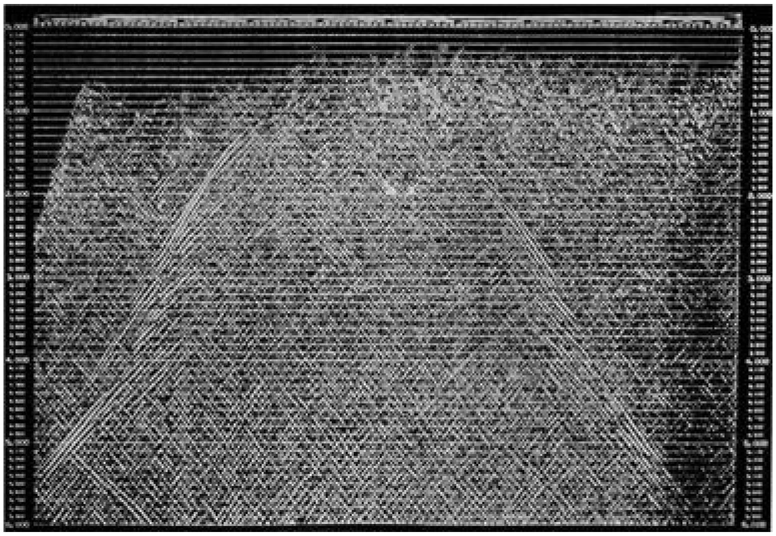

By increasing the dip range to 45 to 60 degrees, Figure 3-46 shows that, in fact, there are reflections in this data set from beds that dip in excess of 45 degrees. What is more important is that these reflections cannot be seen in a typical stack which has not been dip-moveout corrected. Thus, if they are not imaged in a traditional stack, we cannot be expected to image them on post-stack migrated sections.

Figure 3-46. Stack of the data using an assumed dip of 52.5 degrees. At the bandwidth of these data the effect is to stack everything between 45 and 60 degrees of dip.

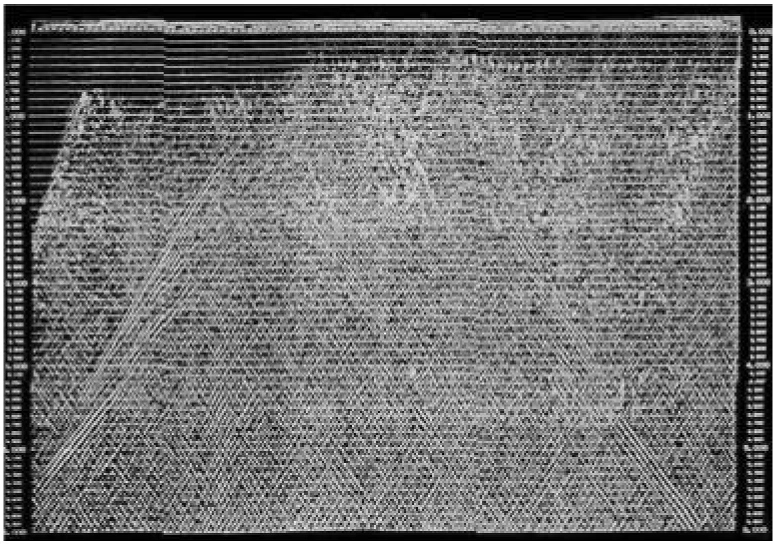

Figure 3-47 is a linear stack of the 15 to 60 degree dipping events. By stacking the sections from the last three figures, we get an idea of the events that should be in the original NMO-only based stack, but are not visible there. When these are migrated, a much clearer picture of the salt structure appears.

Figure 3-47. The sum of the sections in Figures 3-43 through 3-46.

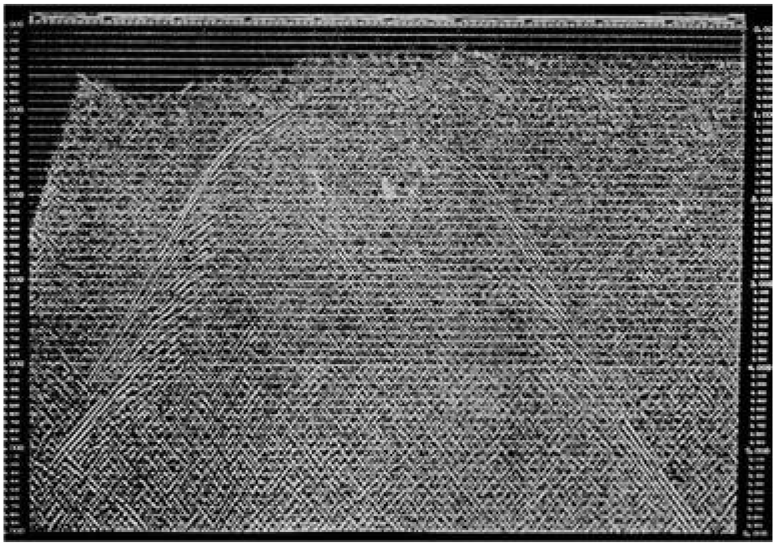

Adding all of the sections together provides the final NMO-DMO corrected stack in Figure 3-48. This DMO corrected data set is much closer to a true zero-offset profile, and now includes reflections from steeply dipping events. Migration of this section will produce a much clearer picture of the salt structure.

Figure 3-48. The sum of the sections in Figures 3-42, and 3-47.

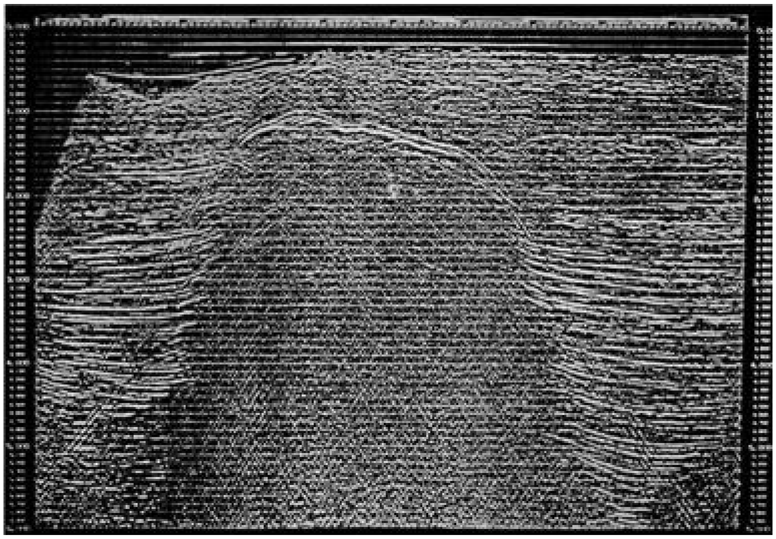

Remarks about DMO

In summary, correcting for dip using DMO partially migrates the data to address the fact that CDP arrival time curves have apparent velocities much faster than flat events. It converts upward sweeping hyperbolas in each and every NMO-corrected CDP into flat events at zero-offset traveltimes. Although it is possible to perform DMO using non-constant velocity fields, in practice, most DMO algorithms are constant velocity methods. They achieve their goals in much the same manner as an ordinary migration, but with much smaller operators. As seen in the earlier figures, it is possible to image dipping events using existing stacking and dip filter methods. What is even more surprising is that constant velocity DMO and even prestack time migration can be accomplished without knowing anything about the velocity.

The NMO-DMO-STACK combination is usually called *partial prestack migration* because it performs three of the four tasks involved in performing a prestack migration. After its application, the only remaining task is to position subsurface events properly. Because NMO-DMO-STACK is relatively cheap, this process played an important early role in improved imaging, and for a time became a standard part of every processing sequence.

However, since most DMO processes are based on constant velocity assumptions, or, at best, $v(z)$ assumptions, they have considerable difficulty producing images below strong velocity variations. Thus, DMO-NMO is a useful tool for imaging steep dips, but is impractical when the objective is subsalt.

With the advent of inexpensive computers and the resulting ability to perform full prestack migration, DMO-NMO no longer reigns as the optimum approach to seismic imaging.

Historical Summary

Absolutely all migration algorithms can be considered to do one or the other of the processes described in this section. Which method we choose to use to explain observed events on imaged sections is pretty much a matter of choice. Diffracting amplitudes over specific curves or smiles is by far the most popular. Nevertheless, it is sometimes helpful to understand the alternative frown-based method. Before this frown-based approach can be fully appreciated, it is necessary to consider the geometrical aspects of data synthesis or seismic modeling. Chapter 3 reviews seismic modeling. Since seismic modeling must of course acquire data in some sense equivalent to normal acquisition procedures, Chapter 4 reviews how seismic data is acquired today.